



HAL
open science

Cryptic sulfur cycling during the formation of giant gypsum deposits

Laetitia Guibourdenche, P. Cartigny, F. Dela Pierre, M. Natalicchio, G. Aloisi

► **To cite this version:**

Laetitia Guibourdenche, P. Cartigny, F. Dela Pierre, M. Natalicchio, G. Aloisi. Cryptic sulfur cycling during the formation of giant gypsum deposits. *Earth and Planetary Science Letters*, 2022, 593, pp.117676. 10.1016/j.epsl.2022.117676 . insu-04035850

HAL Id: insu-04035850

<https://insu.hal.science/insu-04035850>

Submitted on 18 Mar 2023

HAL is a multi-disciplinary open access archive for the deposit and dissemination of scientific research documents, whether they are published or not. The documents may come from teaching and research institutions in France or abroad, or from public or private research centers.

L'archive ouverte pluridisciplinaire **HAL**, est destinée au dépôt et à la diffusion de documents scientifiques de niveau recherche, publiés ou non, émanant des établissements d'enseignement et de recherche français ou étrangers, des laboratoires publics ou privés.



Distributed under a Creative Commons Attribution - NonCommercial - NoDerivatives 4.0 International License

Earth and Planetary Science Letters

www.elsevier.com/locate/epsl

Article history: Received 15 October 2021. Received in revised form 23 May 2022. Accepted 7 June 2022
Available online 1st September 2022

Editor: B. Wing

Volume 593, 1 September 2022, 117676
<https://doi.org/10.1016/j.epsl.2022.117676>

Cryptic sulfur cycling during the formation of giant gypsum deposits

L.Guibourdenche^{a,*}, P.Cartigny^a, F.DelaPierre^b, M.Natalicchio^b, G.Aloisi^a

^aUniversité de Paris, Institut de Physique du Globe de Paris, CNRS, F-75005 Paris, France

^bDipartimento di Scienze della Terra, Università degli Studi di Torino, 10125 Turin, Italy

Keywords: cryptic sulfur cycling, multiple sulfur isotopes, Messinian Salinity Crisis, Primary Lower Gypsum, microbial sulfate reduction, sulfide oxidizing bacteria

Highlights:

- Orbitally-driven hydrological changes controlled sulfur cycling at the onset of Mediterranean Messinian Salinity Crisis.
- In marginal basins, hypoxic to euxinic conditions prevailed during humid period and marls deposition.
- During gypsum formation, microbial sulfate reduction (MSR) and near complete reoxidation of sulfide dominated sulfur cycle.
- More than 80% of the sulfate was cycled through this cryptic sulfur cycling.
- Benthic organic carbon oxidation rates by MSR were comparable to those of the most productive areas of the modern ocean.

Abstract:

Salt giants are large-scale, basin-wide deposits formed sporadically in the geological past, from the early Paleozoic to the late Cenozoic. Their role as sinks for seawater dissolved ions is well known, however the biogeochemical conditions that accompany salt giant formation and their effects on carbon cycling remain poorly constrained. Here we show that massive gypsum deposits of the Mediterranean salt giant – the youngest salt giant on Earth – formed in a particularly dynamic biogeochemical environment controlled by orbitally-driven climate oscillations at the

precessional scale. Using multiple sulfur isotopes combined with a steady-state sulfur cycle model, we show that, prior to gypsum precipitation, more than 80% of its constituting sulfate was first microbially reduced into sulfide, possibly stored as elemental sulfur, and then almost completely microbially reoxidized back to sulfate. This “cryptic” sulfur cycling contemporaneous to gypsum precipitation implies both negligible net sulfate consumption and sulfide production, despite a significant benthic flux of organic carbon remineralized through microbial sulfate reduction. This is the first known evidence of cryptic sulfur cycling in the geological past.

1. Introduction

At the end of the Miocene, starting from about 7.2 Ma, the progressive reduction of water exchanges between the Atlantic Ocean and the Mediterranean Sea dramatically affected Mediterranean environments, increasing their sensitivity to orbitally-driven climate perturbations (Bulian et al., 2021; Hsü et al., 1973; Kouwenhoven et al., 2006). Hydrological restriction of the Mediterranean led to an increase of salinity, a decrease in water column oxygenation and changes in biotic assemblages (Bulian et al., 2021; Cita et al., 1978; Kouwenhoven et al., 2006). Thereafter, the sensitivity of the Mediterranean to precessional cycles became significantly more pronounced, and in turn greatly impacted the biogeochemistry of the basins (Natalicchio et al., 2019; Sabino et al., 2021). This has been recorded as cyclical deposition of sapropel/diatomite-rich marls (Krijgsman et al., 1999) and marl/carbonate alternations (Mancini et al., 2021) corresponding to periods of summer insolation maxima and minima, respectively. Lithological cyclicity is accompanied by variations in the size and abundance of fossils of marine fauna (Mancini et al., 2021), as well as oscillations in the composition and isotopic signature of lipid biomarkers (Natalicchio et al., 2019; Sabino et al., 2020). Together, this evidence suggests the existence of a precessional-scale alternation between a highly productive/stratified water column and a vertically mixed water column.

The progressive intensification of hydrological restrictions between the Atlantic and the Mediterranean culminated at 5.97 Ma with the onset of evaporite precipitation that marked the beginning of the Messinian Salinity Crisis (MSC). During the first phase of the MSC, up to 220 m of cyclical alternations of gypsum and organic-rich deposits (characteristic of arid and humid periods, respectively) forming the Primary Lower Gypsum (PLG) unit (Fig. 1) accumulated in the shallow part of marginal to intermediate depth basins of the Mediterranean (Lugli et al., 2010; Raad et al., 2021; Roveri et al., 2014). During this time, marginal and intermediate depth basins still received significant marine water inputs, as indicated by the $^{87}\text{Sr}/^{86}\text{Sr}$ and S of gypsum and by the occurrence of marine biota (Lugli et al., 2007, Lugli et al., 2010 and references therein; Pellegrino et al., 2021; Reghizzi et al., 2018).

During humid periods of precession cycles, non-evaporitic interbeds deposited in stratified basins where N₂-fixing bacteria significantly contributed to primary productivity (Isaji et al., 2019) and anoxygenic phototrophic bacteria populated the upper water column (Sinninghe Damsté et al.,

1995). Meanwhile, microbial mats dominated by colorless sulfide oxidizing bacteria (CSB) thrived at the seafloor (Dela Pierre et al., 2014). Anoxygenic phototrophic bacteria and CSB mats develop in modern euphotic zone and benthic boundary respectively. They reoxidize H₂S fluxes produced by microbial sulfate reduction (MSR) back to elemental sulfur or sulfate (Brüchert et al., 2006; Callbeck et al., 2021; Jørgensen, 2021). The presence of sulfide oxidizing metabolisms in both the water column and at the sediment-water interface strongly suggest the prevalence of euxinic conditions during marls/organic-rich shale deposition.

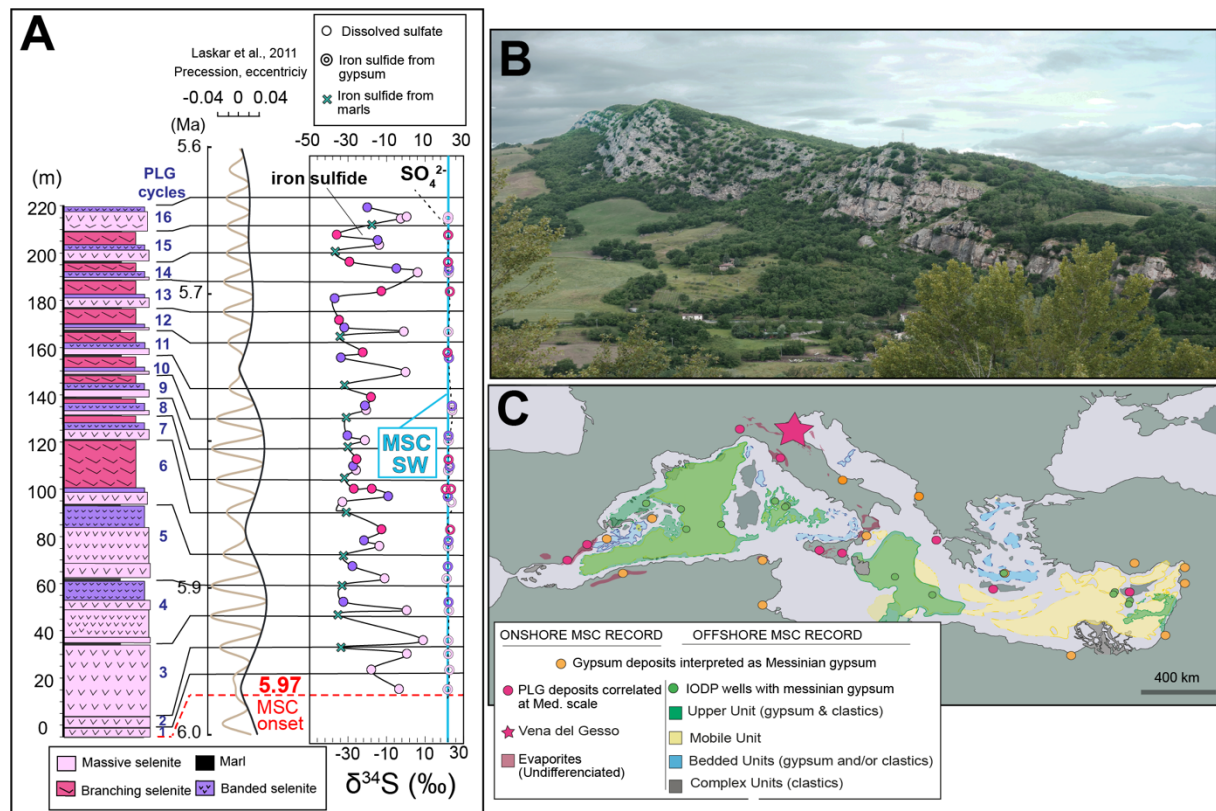


Figure 1 : PLG in the Mediterranean and in the VdG basin.

A. Sulfur $\delta^{34}\text{S}_{\text{SO}_4}$ and $\delta^{34}\text{S}_{\text{SIS}}$ isotopic curve of the PLG succession of the VdG basin, calibrated with the 100ka orbital eccentricity and precession curves (Laskar et al., 2011). Note the nearly invariant $\delta^{34}\text{S}_{\text{SO}_4}$ isotopic variations compared to $\delta^{34}\text{S}_{\text{SIS}}$. **B.** Panoramic view of the 220m thick VdG succession constituted by an alternation of thick gypsum beds and marl intervals (PLG unit). **C.** Distribution of Messinian evaporites in the Mediterranean and the location of the VdG basin (pink star) (see supplementary section 2.1 for references).

Precession maxima (arid periods) were characterized by rapid vertical accretion of bottom grown gypsum crystals (Reghizzi et al., 2018) – which allowed for the relatively good preservation of organic remains (Dela Pierre et al., 2015; Schopf et al., 2012) (Fig. 2). These bottom-grown gypsum crystals make up the bulk of the PLG unit, and contain abundant planktic marine diatoms, implying enhanced primary productivity in the upper water column during gypsum deposition (Dela Pierre et al., 2015; Pellegrino et al., 2021; Schopf et al., 2012).

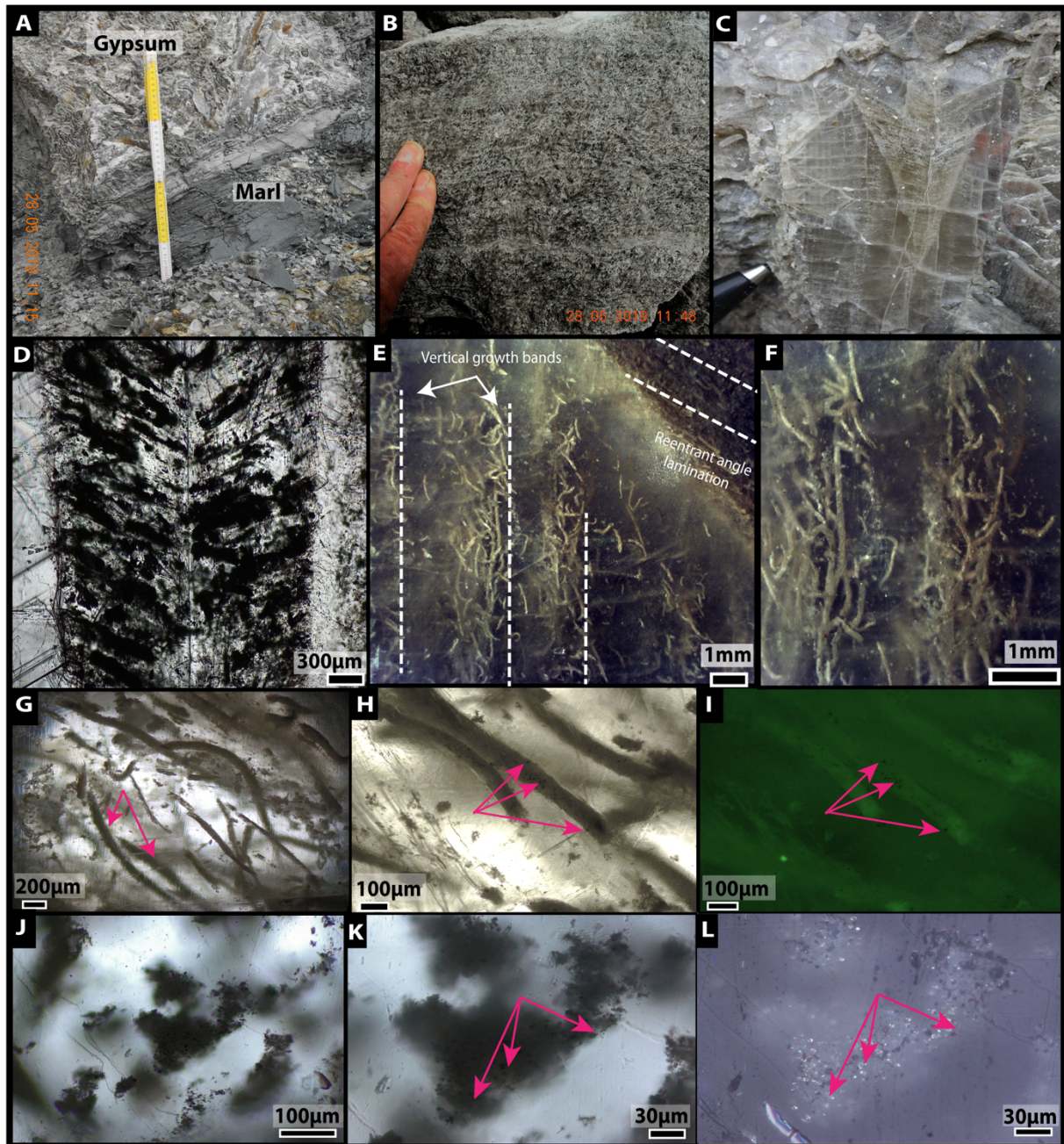


Figure 2: Macro- and microscopic characteristics of VdG PLG gypsum deposits.

A. The basal part of cycle PLG5, composed of a basal dark marly interval followed by a thin whitish carbonate layer, in turn overlain by a gypsum bed consisting of dm-sized vertically oriented selenite crystals (massive selenite lithofacies). **B.** Close-up of the banded selenite facies (cycle PLG7). **C.** Close-up of a vertically oriented selenite crystal (massive selenite lithofacies). Note the turbid portion in the re-entrant angle of the twin. **D.** Photomicrograph (transmitted light) of a twinned selenite crystal showing the lamination in the re-entrant angle of the twin. **E.** Photomicrograph (transmitted light) of a gypsum twin with curved filaments aligned to the vertical growth bands. Lamination in the re-entrant angle is also shown. **F.** Detail of (E) with filaments aligned along a vertical growth band. **G, H, I.** Photomicrographs in transmitted light (G and H) and UV light (I) showing the filaments inside gypsum. Pink arrows show tiny iron sulfide globules within the filaments. Note in (I) the high autofluorescence of the filaments. **J, K, L.** Photomicrographs in transmitted (J, K) and reflected (L) light of clay-rich aggregates in the turbid laminae of gypsum crystals. The aggregates are interpreted as marine snow floccules and contain abundant sulfide grains (arrows).

The molecular fossil assemblages entrapped within Messinian gypsum crystals and their compound specific carbon isotopes are indicative of a diverse microbial community, including marine *Thaumarchaeota* communities living in the upper water column, and sulfate-reducing bacteria and CSB-forming microbial mats at the sea floor (Natalicchio et al., 2022). The latter benthic microbial mats are fossilized within the bottom-grown gypsum in the form of densely-packed networks of filamentous structures (“spaghetti-like” structures) together with pyrite and dolomite, implying that MSR activity occurred during gypsum formation (Dela Pierre et al., 2015; Natalicchio et al., 2022; Panieri et al., 2008; Schopf et al., 2012) (Fig. 2D-I).

Together, these petrographic and geochemical observations point towards a highly dynamic sulfur cycle during PLG formation, with sulfur cycled amongst microbial sulfate reducers and sulfide-oxidizing bacteria, as well as precipitated in its oxidized form as gypsum ($\text{CaSO}_4 \cdot 2\text{H}_2\text{O}$).

Marine carbon and sulfur cycles are tightly linked, with MSR driving the remineralization of between 12 and 65% of the organic carbon flux to the seafloor (Bowles et al., 2014; Bradley et al., 2020; Canfield et al., 2005). Constraining sulfur cycling during the formation of giant sulfate deposits is therefore critical to understand their significance for the carbon cycle. The accumulation of large gypsum deposits – comparable to the Mediterranean PLG- are known to greatly affect the long term carbon cycle and atmospheric oxygen levels by the removal of substantial amount of Ca^{2+} and SO_4^{2-} ions from the ocean, (e.g. Halevy et al., 2012; Shields and Mills, 2020). However, the role of associated MSR and sulfide oxidation on carbon and sulfur cycles of basins where gypsum formed has been overlooked.

This complex sulfur cycling during PLG formation is likely to have been widespread across Mediterranean marginal basins (Natalicchio et al., 2022; Pellegrino et al., 2021)) and raises fundamental questions about the biogeochemical dynamic of these basins, including for instance: (i) What was the relative importance of microbially driven reduction of sulfate and reoxidation of sulfide, compared to the burial of sulfate through gypsum precipitation? (ii) How did sulfur cycling impact carbon cycling in Messinian Mediterranean marginal basins? (iii) How does this ancient system compare with modern marine environments?

In this study, we investigated the most complete PLG succession of the Mediterranean area in the Vena del Gesso basin (VdG) (Northern Apennines, Italy) (Fig. 1b). MSR and re-oxidative sulfur cycling result in specific multiple sulfur isotopes signatures, providing a tool to disentangle the relative influence of concurrent sulfur redox processes (Johnston et al., 2008; Ono et al., 2006). Therefore, to constrain the sulfur biogeochemical cycle during PLG deposition, we carried out measurements of multiple sulfur isotope ratios ($^{34}\text{S}/^{32}\text{S}$ and $^{33}\text{S}/^{32}\text{S}$) on gypsum sulfate and reduced sulfur minerals which co-precipitated with gypsum or that we extracted from marls, coupled to the measurement of oxygen isotopes of gypsum sulfate ($^{18}\text{O}/^{16}\text{O}$). This approach

enabled us to estimate the relative fluxes of sulfide and sulfate in the basin and in turn to estimate the gross flux of organic carbon involved in MSR activity. In modern settings, this is typically achieved with incubation experiments and/or analyses of pore water geochemical profiles – tools that are not available when studying the rock record.

2. Geological setting

The PLG was deposited during the first stage of the MSC (5.97-5.60 Ma) in shallow to intermediate marginal basins of the Mediterranean, including southern Spain, Italy, Hellenic arc and Cyprus arc (Krijgsman et al., 1999; Lugli et al., 2010 and references therein) (Fig. 1c). This unit was deposited in approximately 380 kyrs (Roveri et al., 2014) and is formed by lithological cycles consisting of organic-rich (marls, shale and carbonate)/gypsum couplets (Fig. 1a). The deposition of these interbeds was controlled by precession-driven climate oscillations (Lugli et al., 2010; Roveri et al., 2014). Tuning of the lithological cycles to the astronomical reference curve (Fig. 1a) allows the precise dating of each cycle and bed by bed correlation of the PLG unit at the Mediterranean scale (see the pink dots in Fig. 1c) (Krijgsman et al., 1999; Roveri et al., 2014). Here we studied the VdG in the Northern Apennines (Italy) that exposes the most complete succession of PLG deposits in the whole Mediterranean area (Fig. 1b). Each PLG cycle of the VdG basin starts with a thin (dm to m thick) organic matter-rich (total organic carbon from 0.2 to 3.1%; Lugli et al., 2007) marly bed (Fig. 2a).

The thin marly beds are followed in each PLG cycle by a 4 to 30 m thick bed of primary gypsum (Fig. 2a). The gypsum beds of the first three cycles (PLG1 to PLG3) are mostly composed of bottom-grown, vertically oriented, twinned selenite crystals (up to 2.5 m high) of the massive selenite lithofacies (Lugli et al., 2010).

Starting from the gypsum beds of the 4th PLG cycle, the massive selenite lithofacies is followed upwards by the banded selenite lithofacies composed of less than 10 cm-thick crusts of bottom-grown twinned gypsum crystals separated by thin carbonate laminae possibly reflecting cyclical fluctuation of the gypsum saturation interface (Lugli et al., 2010) (Fig. 2b).

From the 6th PLG cycle to the top of the section, massive and banded selenite are followed by the branching selenite lithofacies consisting of cm-sized clear bottom-grown selenite crystals growing inclined or horizontally and grouped together in nodules or lenses separated by thin fine grained carbonate or gypsum laminae (Lugli et al., 2010). The absence of karst features in any of these lithofacies suggests that PLG gypsum are fully subaqueous deposits formed in a basin permanently covered by waters supersaturated with respect to gypsum.

3. Isotopes to decipher sulfur cycling

3.1. δ³⁴S and δ¹⁸O of sulfate

The sulfur and oxygen stable isotope compositions of pore water dissolved sulfate are frequently used to investigate the biogeochemical sulfur cycling in modern marine sediments (Aller et al., 2010; Blonder et al., 2017; Gilhooly et al., 2016). These stable isotopic compositions are expressed in delta (δ) notations, representing the deviation of ³⁴S/³²S or ¹⁸O/¹⁶O ratios from international VCDT and SMOW standards respectively:

$$\delta(\text{‰}) = \left(\frac{R_{\text{measured}}}{R_{\text{standard}}} - 1 \right) \times 1000 \quad (1)$$

With R_{measured} corresponding to the measured ³⁴S/³²S or ¹⁸O/¹⁶O ratios and R_{standard} corresponding to the VCDT ³⁴S/³²S ratio or SMOW ¹⁸O/¹⁶O ratio.

Sulfate-reducing microbes preferentially metabolize ³²S- and ¹⁶O-bearing dissolved sulfate. Therefore, as dissolved sulfate concentration decreases and hydrogen sulfide concentration increases, residual pore-water sulfate is progressively enriched in ³⁴S and ¹⁸O (Fig.3) (Brunner et al., 2005).

However, the effect of MSR on sulfate and hydrogen sulfide concentration profiles and isotopic compositions can be obscured by re-oxidative processes; this happens because ³⁴S-depleted sulfur metabolized by MSR is re-injected back into the ³⁴S-enriched sulfate pool with little or no fractionation (Fig.3). This results in a smaller net enrichment of dissolved sulfate δ³⁴S due to microbial sulfate reduction, and a lower net production of sulfide/consumption of sulfate. Importantly, if all the hydrogen sulfide produced by MSR is entirely re-oxidized back to sulfate (Fig. 3) (Aller et al., 2010; Blonder et al., 2017; Brüchert et al., 2006; Callbeck et al., 2021), the sulfur cycle is “cryptic” – since there is no net isotopic effect on the δ³⁴S isotopic composition. Furthermore, the shift in δ¹⁸O sulfate isotopic values is often so small (<4‰) (Aller et al., 2010; Blonder et al., 2017) that it can be difficult to recognize the effect of cryptic sulfur cycling from natural variability of oceanic sulfate isotopic composition using this isotope system (Fig.3) (Markovic et al., 2016).

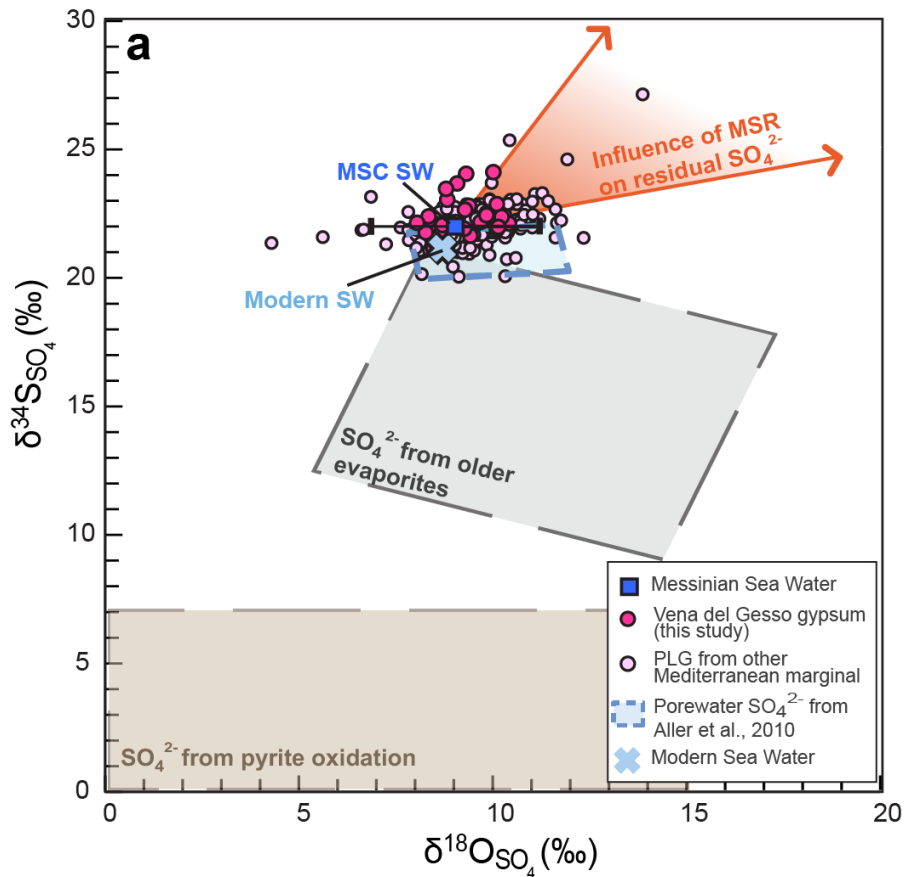


Figure 3: Stable sulfate isotopic composition of VdG gypsum.

$\delta^{34}\text{S}_{\text{SO}_4}$ and $\delta^{18}\text{O}_{\text{SO}_4}$ isotopic composition of the dissolved sulfate ion in equilibrium with the PLG unit from VdG basin (dark pink) and the PLG unit of other marginal basins (light pink) (see Supplementary section 2.1 for references and 2.4 for calibration of $\delta^{34}\text{S}_{\text{SO}_4}$ and $\delta^{18}\text{O}_{\text{SO}_4}$ isotopic data from this study and from the literature). The range of isotope compositions of sulfate-bearing minerals and of sedimentary sulfides are represented as grey and light brown boxes, respectively (see Supplementary section 2.1 for references). The possible range of isotopic composition of riverine inputs is bracketed by the isotopic composition of sulfate-bearing minerals and sedimentary sulfides (see Supplementary section 2.1 for further details on riverine fluxes). The possible evolution of the isotopic composition of residual sulfate during MSR is indicated by the orange shaded area. The isotope composition of sulfate dissolved in top few centimeters of modern marine environments characterized by near complete reoxidation of H_2S is represented by the blue box (Aller et al., 2010).

3.2. Multiple sulfur isotopes

Multiple sulfur isotopes (including ^{32}S , ^{33}S , ^{34}S) have the potential to distinguish biogeochemically distinct hydrogen sulfide re-oxidation pathways occurring concomitantly with MSR – the signal of which might otherwise be obscured using traditional isotope systems (Johnston et al., 2008; Ono et al., 2006; Zhang et al., 2017).

The partitioning of ^{34}S ($^{34}\text{S}/^{32}\text{S}$) relative to ^{33}S ($^{33}\text{S}/^{32}\text{S}$) is predictable under thermodynamic equilibrium. However, intracellular biochemical branching processes will shift the minor ^{33}S sulfur isotope partitioning ($^{33}\text{S}/^{32}\text{S}$) thus resulting in a deviation from the expected

thermodynamic equilibrium relationship (Ono et al., 2006). This deviation is expressed as $\Delta^{33}\text{S}$ where:

$$\Delta^{33}\text{S}_i = \left[\left(\frac{{}^{33}R_{\text{measured}}}{{}^{33}R_{\text{VCDT}}} - 1 \right) \times 1000 \right] - \left[\left(\frac{{}^{34}R_{\text{measured}}}{{}^{34}R_{\text{VCDT}}} - 1 \right)^{\lambda_{\text{eq}}} \times 1000 \right] \quad (2)$$

The measurement of $\delta^{34}\text{S}$ - $\Delta^{33}\text{S}$ thus provides additional information as deviation from thermodynamic equilibrium can be linked to biological fractionation processes and mixing proportions of end-member sulfur species involved in sulfur cycling (Fig. 4) (Ono et al., 2006).

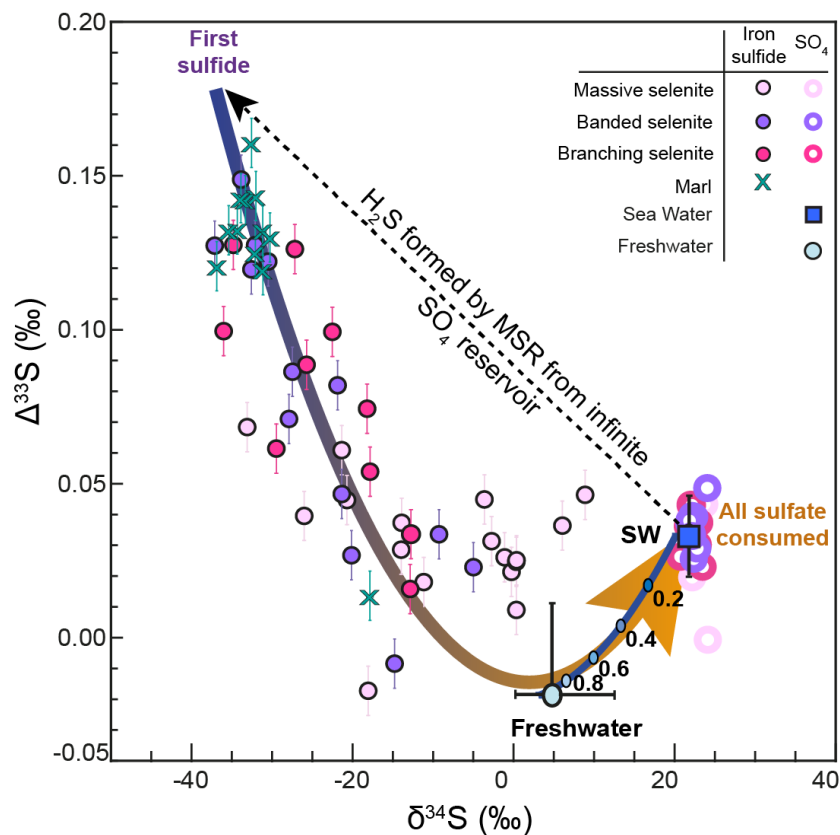


Figure 4. Multiple Sulfur isotopic composition of sulfate and sulfide minerals constituting PLG deposits.

Data points represent the $\Delta^{33}\text{S}$ vs $\delta^{34}\text{S}$ of sulfate and sulfide of gypsum (massive, banded, and branching selenite) and marl samples from the PLG unit of the VdG Basin. The dashed black arrow points to the isotopic composition of the first sulfide formed from oceanic sulfate by MSR considering the most depleted sulfide of marls measured in this study as a representative endmember. The curved arrow represents the calculated trajectory between this first sulfide and a pooled sulfide formed after the complete consumption of the initial sulfate reservoir. The blue line represents mixing of Messinian oceanic sulfate (SW) with the average isotopic composition of modern rivers (Freshwater), with friv = 0 representing the marine endmember and friv = 1 representing the riverine endmember. Note that the contribution of riverine SO_4 to gypsum SO_4 isotopic composition seems negligible.

The deviation from thermodynamic equilibrium is also expressed by the $^{33}\lambda$ notation that defines the relationship between isotopic fractionation for ^{33}S and ^{34}S isotopes among two sulfur species:

$$^{33}\lambda_j = \frac{\ln(^{33}\alpha_j)}{\ln(^{34}\alpha_j)} \quad (3)$$

with λ for thermodynamic equilibrium $^{33}\lambda_{\text{eq}} = 0.515$, and $\alpha_j = x/^{32}\text{R}_{\text{product}}/x/^{32}\text{R}_{\text{reactant}}$, and $x = 33$ or 34 .

Combining the $^{33}\lambda$ and the classical $^{34}\epsilon$ [= $(^{34}\alpha_j - 1) \times 1000$] notations is particularly useful as λ and ϵ fractionation factors are dependent solely on the biogeochemical processes in question (e.g. MSR, biotic or abiotic sulfide oxidation). In addition, the combination of $^{33}\lambda$ and $^{34}\epsilon$ is not sensitive to the absolute isotopic value of the reacting sulfur species (Fig. 5) or the almost invariant temperatures relevant for sedimentary environments (Eldridge et al., 2016).

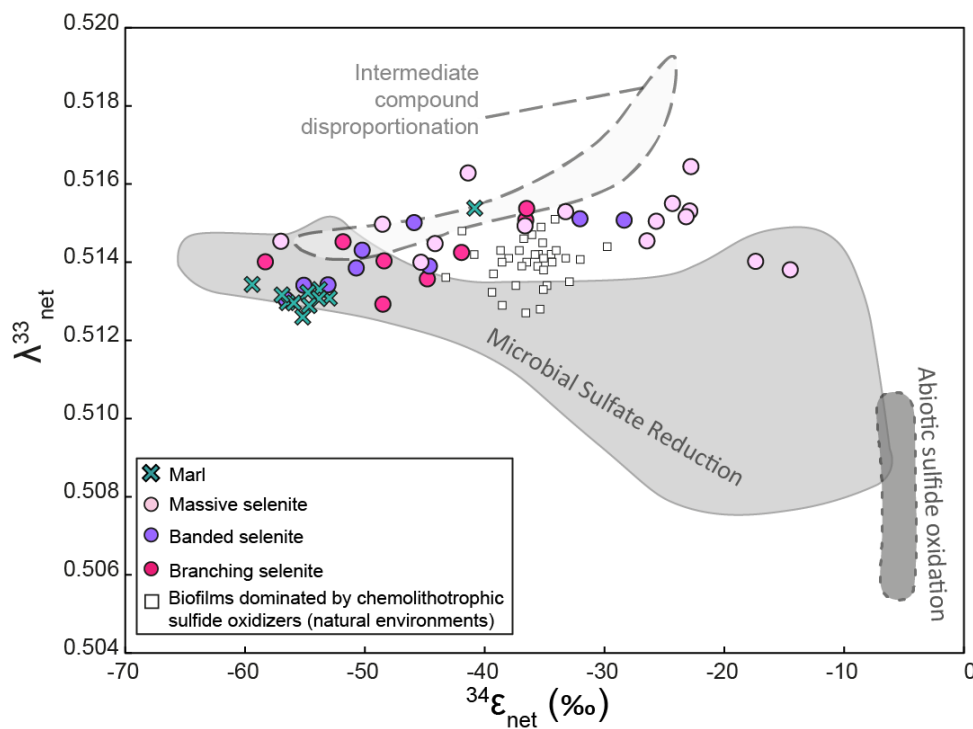


Figure 5: Comparison between fractionation factors determined in laboratory experiments and net fractionations deduced from VdG sulfide and sulfate minerals.

Net fractionation factors $^{34}\epsilon_{\text{net}}$ and $^{33}\lambda_{\text{net}}$ calculated for the gypsum (massive, banded, and branching selenite) and marl samples using the isotope compositions of the sulfate ion in equilibrium with gypsum and the sulfur isotope composition of iron sulfides (dots and crosses) compared with ranges of $^{34}\epsilon$ and $^{33}\lambda$ values obtained in pure cultures of sulfur metabolizing microorganisms (shaded areas). For marls samples, where no gypsum precipitates occur, an isotope composition of the sulfate ion equal to the Messinian ocean value (Masterson et al., 2016) was set, based on the assumption that sulfides from marls were produced through the reduction of oceanic sulfate. See Supplementary section 4.1 for references on data from abiotic sulfide oxidation experiments (dark grey area with black dotted contour),

data from pure cultures with sulfate reducers (light grey area), data from pure culture experiments with sulfur disproportionators and ^{34}S and ^{33}S fractionation factors measured in natural environments populated with biofilms dominated by chemolithotrophic sulfide oxidizers (white squares).

4. Material and methods

A total of 88 samples that are representative of each lithofacies of all cycles from the VdG succession were analyzed (Fig. 1A). Gypsum and marls from PLG cycle 1-2 were sampled in the Monticino quarry (44°13'29"N, 11°45'43"E) whereas cycles 3 to 16 were sampled in the Monte Tondo quarry (44°15'04"N, 11°40'13"E). Care was taken to avoid sampling the weathered surface and visible fractures in order to limit contamination.

4.1. Petrographic analyses

11 oriented samples were taken from the various gypsum lithofacies for petrographic observations. Fifteen petrographic thin sections and 10 thin slices (~1 mm thick) were produced from the most representative samples by cleaving the selenite crystals along the main (010) cleavage planes with a razor blade. These were studied using transmitted, reflected, and UV-visible light microscopy, using a Leika DM 2700 P microscope with excitation filters 340-380 Nm at the Department of Earth Sciences of the University of Torino.

4.2. Oxygen and multiple sulfur isotope analyses

Sulfate from gypsum and iron sulfide from gypsum and marls were first reduced and transformed into Ag₂S by wet chemistry. The multiple sulfur isotope composition was then measured using a MAT-253 mass spectrometer. Oxygen isotopic composition of sulfate from gypsum were measured on samples precipitated as BaSO₄ (the full methods with references are detailed in supplementary material section 1).

4.3. Geochemical modeling

4.3.1. Description of the model

We interpret the multiple S isotope data using a steady-state, 3-box model based on a chemical and isotopic mass balance of sulfur in the SO₄²⁻, S⁰ and H₂S forms. In the model (see Fig. 6) sulfate is provided by oceanic (F_{in}) and riverine inputs (F_{riv}) whereas it is removed from the basin through outflow into the open ocean (F_{out}) or gypsum precipitation (F_{gyp}). In addition, the sulfate can be reduced to hydrogen sulfide by microbial sulfate reduction (F_{msr}), and hydrogen sulfide can be either buried as solid sulfide (F_{is}) or reoxidized (F_{ox}). Sulfide reoxidation (biotic or abiotic) produces sulfate or an intermediate sulfur compound (elemental sulfur or sulfite) (F_{ox}).

Finally, intermediate sulfur compounds can be reoxidized back to sulfate (F_{ox}) or further disproportionated into hydrogen sulfide (F_{dh}) and sulfate (F_{do}) (Fig. 6).

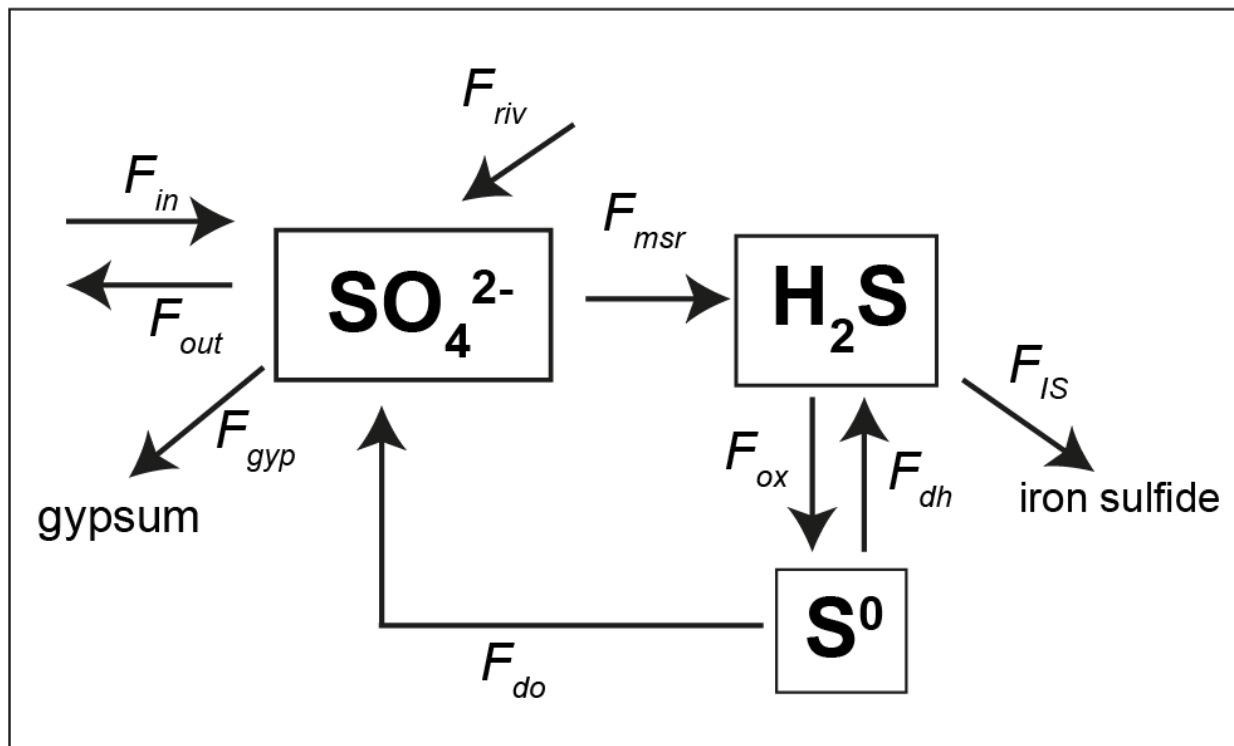


Figure 6: Structure of the numerical model simulating the biogeochemical cycling of sulfur in an idealized marginal basin.

The three boxes correspond to the inventories of sulfate (SO_4^{2-}), sulfide (H_2S) and sulfur with an intermediate oxidation state (sulfite: SO_3^{2-} or elemental sulfur: S^0). The arrows represent the sulfur fluxes described in section 4.4.1.

4.3.2. Fractionation factors

Sulfur redox or phase changes are often associated with a differential partitioning of sulfur isotopes. Therefore, the expressed fractionation ϵ_{net} and λ_{net} between two co-occurring sulfur species of interest (typically sulfate and sulfide) results from the net effect of multiple processes involved in the cycling of these sulfur species (Fig.5). To model the biogeochemical processes at play during the genesis of our samples, we assigned fixed fractionation factors established in pure culture experiments or environmental studies to each of the fractionating process considered in our model (see supplementary section 4.1), with the exception of sulfate reduction that potentially expresses a large range of isotopic fractionation (Gomes and Hurtgen, 2015; Sim et al., 2011b; Wing and Halevy, 2014). In the following paragraph, we detail the approach we chose to simulate fractionation of multiple sulfur isotopes during MSR.

Laboratory experiments and studies of natural environments suggest that there is a first-order control of the specific cellular rate of MSR ($csSRR$) on the extent of sulfur isotopic fractionation during MSR, with fractionation approaching equilibrium values (i.e. $\epsilon_{eq} = -70\%$ and $\lambda_{eq} = 0.515$)

when csSRR reaches minimum values (Sim et al., 2011a; Sim et al., 2011b; Stam et al., 2006) (Fig. 5). The laboratory-observed csSRR at which these relationships have been established are often 1-3 orders of magnitude higher than the csSRR usually reported from natural marine environments (Colangelo-Lillis et al., 2019; Jørgensen, 2021 and references therein). Some authors therefore argue that csSRR in marine environments are so low that cells always express fractionation factors close to equilibrium values ($\epsilon_{MSR} \approx -70\text{‰}$ and $\lambda_{MSR} \approx 0.515$) (e.g. Masterson et al., 2018). These authors propose that when apparent fractionation factors between sulfate and sulfide (ϵ_{net} and λ_{net}) deviate from equilibrium values, the deviation is mainly a consequence of sulfide pooling produced by sedimentary or early diagenetic processes (see section 5.2.2.1 for further explanations on this mechanism) (Masterson et al., 2018).

$\epsilon_{net} > -70\text{‰}$ and $\lambda_{net} < 0.515$ are often observed in systems where depositional controls are absent or negligible, implying that natural populations of microbial sulfate reducers can produce a large range of isotopic fractionations (Colangelo-Lillis et al., 2019; Gilhooly et al., 2016; Gomes and Hurtgen, 2015 and references therein; literature review in Sim et al., 2011a). In addition, modeling studies also suggest a first order control of csSRR on fractionation during MSR (Bradley et al., 2016; Wing and Halevy, 2014). However, secondary factors independent from csSRR might also influence the extent of isotopic fractionation expressed during MSR (e.g. Bradley et al., 2016; Brüchert et al., 2001; Colangelo-Lillis et al., 2019; Stam et al., 2006; Wing and Halevy, 2014). Although it is not within the scope of this work to reconcile laboratory experiments with field observations and modelling studies, we point out that the correct estimation of csSRR in natural environments (in mol.cell⁻¹.day⁻¹) relies on: (i) a precise estimate of the number of physiologically active sulfate reducing microbial cells, and (ii) the absence of significative reoxidative sulfur cycling. Any overestimation of active MSR cell abundance (Colangelo-Lillis et al., 2019) and/or underestimation of the rate of sulfide oxidation (Jørgensen, 2021; Treude et al., 2021) might lead to a large underestimation of csSRR. It is possible that the current observed range of csSRR in natural environments is biased towards low rates (Jørgensen, 2021), whereas csSRR is directly measured in pure culture experiments that allow the entire range of possible MSR-induced fractionations to be explored (Sim et al., 2011a; Sim et al., 2011b) (Fig.5).

We consider that pure culture experiments linking fractionation factors ϵ_{MSR} and λ_{MSR} to csSRR provide a valid first order approximation of the behavior of sulfur isotope fractionation to MSR. We used a nonlinear regression model in combination with pure culture experiment ϵ_{MSR} , λ_{MSR} and csSRR data to model the full range of MSR fractionation potentially expressed in natural environments (see supplementary 4.2 for detailed explanation). This approach does not consider the other environmental controls on MSR induced isotopic fractionation and should not be used to directly deduce a csSRR from our data but provide a simplistic way to model the ϵ_{MSR} and λ_{MSR} co-variation produced by MSR.

5. Results and discussion

Iron sulfides are found in all investigated gypsum and marl samples from VdG (Fig. 1A, supplementary section 3.1, and previously by Panieri et al. (2008) and Sinninghe Damsté et al. (1995)). Iron sulfides form from the reaction of hydrogen sulfide produced by MSR with reactive iron, thus providing evidence for an active biogeochemical sulfur cycle during the first phase of the MSC.

5.1. Marl interbeds

In marls, iron sulfides display the smallest variability, the lowest $\delta^{34}\text{S}_{\text{IS}}$ (average $-32 \pm 5 \text{‰}$ vs CDT (1σ)) and the highest $\Delta^{33}\text{S}_{\text{IS}}$ (average $0.12 \pm 0.04 \text{‰}$ (1σ)) of all analyzed samples (Figure 1A, Figure 4, supplementary section 3.1). These isotopic values are typical of environments where the amount of available dissolved sulfate for MSR is effectively infinite (e.g. Gomes and Hurtgen, 2015; Johnston et al., 2008). We calculated net isotope fractionation factors $34\epsilon_{\text{net}}$ and $33\lambda_{\text{net}}$ for marl samples considering a sulfate isotopic composition equal to that of the Messinian Ocean, based on the assumption that sulfide in marls was produced via the reduction of oceanic sulfate.

Marls fractionation factors fall within the MSR field (Figure 5.) and in fact represent the set of samples in this study that are the closest to the maximal fractionation expressed during MSR, with similar values to what is observed in modern organic-rich hypoxic to euxinic basins (e.g. Gomes and Hurtgen, 2015; Johnston et al., 2008). This is consistent with previous observations suggesting that these organic rich marls formed under stratified and frequently euxinic water columns (Dela Pierre et al., 2014; Isaji et al., 2019; Lugli et al., 2010; Sinninghe Damsté et al., 1995) (Fig.7a).

5.2. Gypsum beds

5.2.1. Petrographic evidence: co-occurrence of MSR and sulfide oxidation

Petrographic analyses of gypsum samples show that iron sulfides are associated with either marine snow floccules (Figure 2.J-L) or filamentous fossils (Figure 2.I-G), which are dominant components of the VdG gypsum (Natalicchio et al., 2022; Panieri et al., 2008; Schopf et al., 2012) and PLG deposits of other Mediterranean marginal basins (Dela Pierre et al., 2015; Natalicchio et al., 2022). The origin of the filaments has been disputed. They have been interpreted as cyanobacteria (Panieri et al., 2008), even if they are generally larger ($\sim 70 \mu\text{m}$ diameter) than most modern cyanobacterial filaments (Schopf et al., 2012 and references therein) (Figure 2. E-I). Moreover, the fact that filaments are mostly located both in the reentrant angle and along the vertical growth bands ((Figure 2.D-F) suggests that they formed a benthic mat located at the gypsum-bottom water interface and that filamentous microorganisms were entrapped within

gypsum in their living position, rather than after having settled from the photic zone to the basin floor (Dela Pierre et al., 2015; Schopf et al., 2012). Finally, the presence of intracellular iron sulfide globules ((Figure 2.G-I) - interpreted as resulting from diagenetic transformation of sulfur globules (Dela Pierre et al., 2015; Schopf et al., 2012) – is a diagnostic feature of benthic giant CSB. Such observations confirm the affiliation of the observed filament networks to chemotrophic microbial mats where both MSR and sulfide oxidation were active (Dela Pierre et al., 2015; Natalicchio et al., 2022; Schopf et al., 2012).

5.2.2. Isotopic composition of PLG gypsum deposits

5.2.2.1. *Influence of syn-depositionnal or early diagenetic processes on multiple sulfur isotopes*

The sulfur isotopic composition of the dissolved sulfate ion in equilibrium with the VdG gypsum ranged between 20.73 and 24.11 ‰ for $\delta^{34}\text{SSO}_4$, and between -0.001 and 0.049 ‰ for $\Delta^{33}\text{SSO}_4$ (Fig. 1A,3,4 Supplementary Table S2). These values fall within a narrow range that is centered around the isotopic composition of the Messinian Ocean dissolved sulfate ion ($\delta^{34}\text{SMESS}=22.2\pm 0.2$ ‰ and $\Delta^{33}\text{SMESS}=0.035\pm 0.013$ ‰) (Masterson et al., 2016) (Figure 1.A, 3, 4).

In contrast to the almost invariant isotopic composition of the sulfate, the iron sulfides entrapped in the same gypsum samples display a large range of isotopic compositions ($-36 < \delta^{34}\text{S}_{\text{IS}} < +9$ ‰ and $-0.017 < \Delta^{33}\text{S}_{\text{IS}} < 0.149$), from high $\Delta^{33}\text{S}_{\text{IS}}$ – low $\delta^{34}\text{S}_{\text{IS}}$, which is comparable to that of iron sulfides contained within marl deposits intercalated to the gypsum beds, to close to zero $\Delta^{33}\text{S}_{\text{IS}}$ and $\delta^{34}\text{S}_{\text{IS}}$ (Figure 1.A, 4 and Supplementary section 3.1 and 3.2).

The theoretical maximal sulfur isotopic fractionation induced by MSR ($\epsilon_{\text{MSR}}\approx -70$ ‰) generate sulfide isotope values of ~ -50 ‰ in $\delta^{34}\text{S}_{\text{IS}}$ when the sulfate used during MSR has a marine isotopic composition ($\sim +20$ ‰). In some cases, the isotopic composition of iron sulfide differs substantially from this maximal estimate due to sulfide pooling controlled by local diagenetic or sedimentological processes (e.g. Masterson et al., 2018; Pasquier et al., 2021b; Pasquier et al., 2017). Sulfide pooling occurs when the rate at which sulfate is consumed (and sulfide is produced) in a given environment overcomes the rate at which the sulfate pool is replenished by diffusion from the overlying sulfate-rich water column (Fike et al., 2015). This leads to the progressive enrichment in ^{34}S of the residual sulfate and produces sulfide pools following a Rayleigh-type distillation. The observed isotopic difference (ϵ_{net}) between oceanic sulfate values and sedimentary sulfide is therefore smaller than the actual MSR induced fractionation (ϵ_{MSR}) because the pool of sulfate used by MSR is not oceanic sulfate (and therefore replenishable) but an aliquot of it (and therefore finite). For example, sulfide pooling has been proven to control the isotopic composition of sulfides in cases where sedimentation rates are so high that porewater sulfate is disconnected from the overlying water column (Pasquier et al., 2017), or where high

concentrations or reactivities of organic matter in sediments results in efficient sulfate depletion due to MSR (Pasquier et al., 2021b). In other cases, iron sulfides enriched in ^{34}S are observed due to sediment mixing by oceanic currents or bioturbation bringing together pooled ^{34}S -enriched sulfide with newly formed ^{34}S -depleted sulfide (Fike et al., 2015; Pasquier et al., 2021a).

The petrographic evidence and isotopic signature of gypsum and co-occurring iron sulfides from the VdG deposits infers particular depositional settings that exclude the role of sulfide pooling in shaping the sulfur isotopic signatures measured in this study. We detail the reasoning in the following paragraphs.

In the $\delta^{34}\text{S}$ vs $\Delta^{33}\text{S}$ space, part of the gypsum iron sulfide samples fall along a curve (see the curved arrow in Figure 4.) consistent with the mixing of two sulfur reservoirs (Ono et al., 2006): (i) sulfide formed by MSR from an infinite, undistilled sulfate reservoir where the isotopic fractionation between sulfate and sulfide is close to equilibrium (corresponding here to the most depleted sulfide measured in this study with $\delta^{34}\text{S} \sim -40\text{‰}$ and positive $\Delta^{33}\text{S} \sim +0.17\text{‰}$) and (ii) what would seem to be pooled sulfide produced by the consumption of SO_4 by MSR (and therefore characterized by an isotope composition that tends to approach that of initial, unreacted sulfate, as sulfate is consumed) (Ono et al., 2006; Zhang et al., 2017).

To test the possible influence of sulfide pooling on the isotopic composition of our samples, we applied a Rayleigh type distillation to estimate the relative amount of sulfate necessary to be consumed to reproduce our data. We calculated that 55 to 95% of the sulfate reservoir should be consumed by MSR to reproduce the ^{34}S -enrichment in our samples in which $\delta^{34}\text{S}_{\text{IS}}$ falls between -20‰ and +10‰ (capturing 50% of the iron sulfides measured) (Figure 4.). We tested this with fractionation factors of -70‰ (i.e., the thermodynamic equilibrium fractionation between sulfate and hydrogen sulfide) and -58‰ (i.e., the net fractionation between the lowest measured $\delta^{34}\text{S}_{\text{IS}}$ and its corresponding $\delta^{34}\text{S}_{\text{SO}_4}$).

Such significant consumption of sulfate should either: (i) have led to the undersaturation of bottom waters with respect to gypsum, thus resulting in partial dissolution of the underlying gypsum, or (ii) have produced a substantial ^{34}S -enrichment of the isotopic signature of the residual sulfate pool preserved in gypsum. However, detailed petrographic studies of VdG gypsum here and in both Reghizzi et al. (2018) and (Panieri et al., 2008) indicate that gypsum laminae have grown continuously without being interrupted by dissolution episodes (Figure 2.) and no substantial ^{34}S -enrichment of the gypsum phase (Figure 1., 3., and 4) have been observed in our samples, consistently with Lugli et al. (2007).

Finally, a drastic drop in the sulfate concentration within CSB mats seems highly unlikely because (i) mats hosting CSB grew on gypsum lamina (Figure 2.) that would provide an effectively infinite source of sulfate upon gypsum undersaturation; however, no inter-laminae dissolution features

are observed as stated above, and (ii) CSB can efficiently oxidize reduced sulfur to SO_4 (Brüchert et al., 2006; Callbeck et al., 2021; Treude et al., 2021).

The combined action of biogeochemical production of SO_4 by CSB, together with an infinite SO_4 reservoir (represented by the gypsum substrate below the mat and the water column above the mat), exclude the possibility of a large reservoir effect due to sulfate consumption. We therefore conclude that pooling effects did not modify the isotopic composition of our samples.

5.2.2.2. *Sulfide and sulfate mineral formation from the same sulfur pool*

An alternative scenario is therefore needed to explain the large range of variation in $\delta^{34}\text{S}$ isotopic composition of iron sulfides entrapped in gypsum ($-58\text{‰} < \epsilon_{\text{net}} < -14\text{‰}$). Previous nano-SIMS studies have shown that the isotopic composition of sulfides measured within microbial mats varied with depth due to variable sulfate concentration and/or csSRR within the mat (Fike et al., 2008). The isotopic compositions reported here, however, represent bulk measurements for each PLG gypsum cycle, and therefore are reflective of the most prominent processes governing the partitioning of sulfur species in the mat within several "generations" of CSB hosting mat (rather than local intra-mat conditions).

In the PLG deposits studied here, gypsum is a bottom-grown precipitate and is composed of an alternation of clear and turbid laminae (Figure 2. D-F). The mm-thick turbid laminae entrap filaments of CSB in close association with marine snow flocules rich in organic matter and iron sulfide minerals, (Figure 2. D-L). This suggests that sulfate reduction and sulfide reoxidation by CSB bacteria occurred in the same space, most probably in the mat adhering to the previously formed gypsum laminae (Figure 2. D-F, Figure 7. B,C). Since the surface underlying each successive layer of microbial mat was gypsum, the bottom boundary of the MSR zone was likely restricted to the base of the microbial mat, and sulfides were produced in-situ with no contribution of hydrogen sulfide diffusing from below (Figure 7C).

Accordingly, iron sulfides co-precipitated with gypsum have multiple sulfur isotopic values ($\Delta^{33}\text{S}_{\text{IS}} - \delta^{34}\text{S}_{\text{IS}}$) that neither reflect the overall water column conditions of the basin nor the bottom water sulfur cycling, but instead provide information on the dynamic of sulfur cycling within the mats permineralized in gypsum.

We interpret the $\Delta^{33}\text{S}_{\text{IS}} - \delta^{34}\text{S}_{\text{IS}}$ signature of iron sulfides as reflecting isotope fractionation processes associated with the biogeochemical sulfur cycle during gypsum precipitation (Figure 7). The same pool of sulfate was used to precipitate gypsum and to produce hydrogen sulfide through MSR. It is important to note that the particular depositional conditions under which the VdG iron sulfide and gypsum minerals co-precipitated are drastically different from what is observed in traditional marine sediments settings ((Figure 7.B, C).

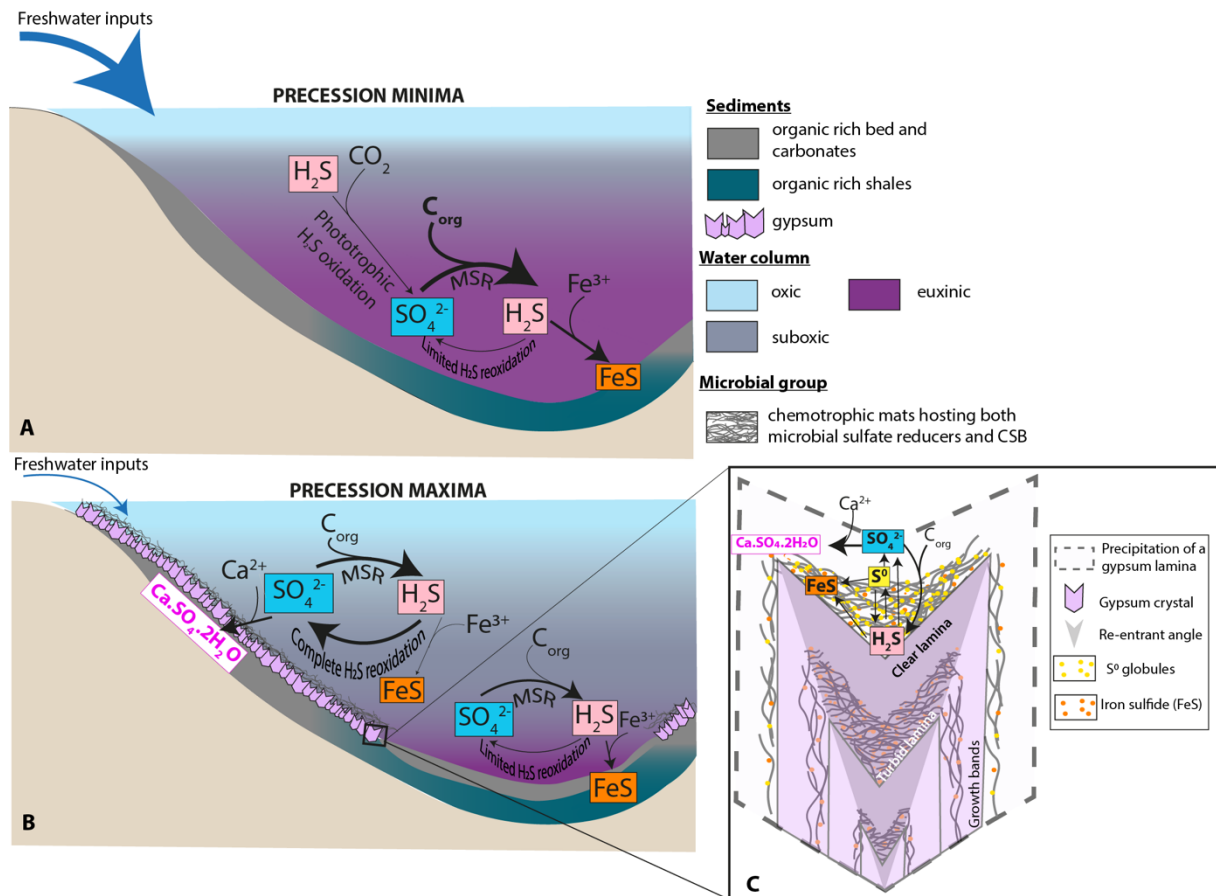


Figure 7. Schematic representation of the biogeochemical conditions that accompanied PLG deposition. (A) Deposition of organic rich marls during humid phases (precession minima). (B) Deposition of gypsum in the margins and marls in the depocenter during arid phases (precession maxima). The relative size of the arrows represents the approximate magnitude of fluxes. (C) Details of a gypsum twin.

e

5.2.2.3. Paired sulfate-sulfide isotopes as a fingerprint of reoxidative sulfur cycling

The combination of iron sulfide and gypsum co-precipitation and the absence of sulfide pooling influence here allows for the calculation of net fractionation factors ($^{34}\epsilon_{\text{net}}$ - $^{33}\lambda_{\text{net}}$) between sulfate from gypsum and their coeval iron sulfides in our samples.

These net sulfate-sulfide isotope fractionation factors fall between the range of isotopic fractionations observed in pure cultures of microbial sulfate reducers and those observed in pure cultures of sulfur disproportionators (Figure 5). Therefore, we conclude that a process characterized by $^{33}\lambda$ higher than maximal $^{33}\lambda_{\text{MSR}}$ (>0.515) contributed, together with MSR, to define the isotopic composition of at least a part of the gypsum samples.

The candidate processes include biotic H_2S oxidation ($^{33}\lambda_{\text{H}_2\text{S}-\text{SO}_4\text{ox}} = 0.513-0.529$) and intermediate oxidation state sulfur disproportionation ($^{33}\lambda_{\text{H}_2\text{S}-\text{SO}_4\text{disp}} = 0.514-0.528$) (see Table 2.1). In support of this idea, the ten most ^{34}S -enriched samples ($\delta^{34}\text{S}_{\text{S}}$ between -20 and $+8$ ‰ and $\Delta^{33}\text{S}_{\text{S}}$ between

0.01 and 0.05‰) deviate from the mixing curve ((Figure 4) that assumes sulfide originating from a reservoir affected by sulfide pooling. Indeed, the contribution from a pooled sulfide reservoir is highly unlikely (see section 5.2.2.1), implying that this deviation is due to an additional sulfide pool. This alternative sulfide pool has a higher $\Delta^{33}\text{S}_{\text{IS}}$ than seawater (0.035‰), and was possibly produced by disproportionation, as proposed in studies where a similar deviation was observed (Zhang et al., 2017).

This scenario is fully supported by the occurrence of two distinct sulfide pools in gypsum ((Figure 2., 4): the first one, associated with marine snow floccules ((Figure 2.J-L), was produced by MSR in an infinite sulfate reservoir; the second, associated with remains of sulfide oxidizing bacteria ((Figure 2G-I), results from the reoxidative part of the sulfur cycle.

In support of the significant occurrence of reoxidative sulfur cycling, the sulfur and oxygen isotopic composition of the dissolved sulfate ion in equilibrium with the VdG gypsum ($20.73 < \delta^{34}\text{S}_{\text{SO}_4} \text{‰ vs CDT} < 24.11$; $-0.001 < \Delta^{33}\text{S}_{\text{SO}_4} \text{‰ vs CDT} < 0.049\text{‰}$; $8.01 < \delta^{18}\text{O}_{\text{SO}_4} \text{‰ vs SMOW} < 10.84$) (Figure 1., 3, 4 and supplementary Table S2) fall within a restricted range centered around the isotopic compositions of the dissolved sulfate ion of the Messinian Ocean ($\delta^{34}\text{S}_{\text{MESS}}=22.2\pm 0.2 \text{‰}$ and $\Delta^{33}\text{S}_{\text{MESS}}=0.035 \pm 0.013 \text{‰}$) (Masterson et al., 2016) and $\delta^{18}\text{O}_{\text{MESS}}=9\pm 2\text{‰}$ (Markovic et al., 2016)), implying negligible contributions from freshwater sulfate (Figure 1,3,4). Together with the very low iron sulfide concentration in gypsum (supplementary Figure S1), the lack of ^{34}S and ^{18}O enrichment of sulfate characteristic of MSR (Kah et al., 2001; Melegy and Ismael, 2013) implies either that MSR activity during gypsum deposition was limited, or that the re-oxidation of sulfide into sulfate was nearly complete, i.e. the sulfur cycle was cryptic (Aller et al., 2010; Blonder et al., 2017) (Figure 3.).

5.3. Modelling multiple sulfur isotopes in the Vena del Gesso basin.

5.3.1. Modeling strategy

To evaluate the importance of microbially-induced sulfide oxidation and to test the hypothesis of cryptic sulfur cycling, we quantified the relative contribution of biogeochemical processes in defining the multiple S isotope compositions of the VdG samples applying the numerical model described in section 4.3.

In order to find a best fit to our data we tested several scenarios of sulfur redox cycling (see supplementary section 9), each one characterized by different relative sulfur fluxes (controlled by dimensionless f_x parameters defined in supplementary section 5) and by a combination of distinct isotope fractionations (see Table S3) according to the following scenarios:

- (i) MSR only (without reoxidation of sulfide).
- (ii) MSR coupled to direct abiotic oxidation of sulfide to sulfate.
- (iii) MSR coupled to phototrophic oxidation of sulfide to sulfate or elemental sulfur.
- (iv) MSR coupled to partial oxidation of sulfide to elemental sulfur by chemolithotrophs and subsequent disproportionation of elemental sulfur.
- (v) MSR coupled to partial oxidation of sulfide to sulfite and subsequent disproportionation of sulfite.

Supplementary section 9 provides full details on the modelling and results of the various biogeochemical scenarios. In all scenarios (i) to (v), the entire range (from 0 to 1) of f_{ox} was explored (f_{ox} refers to the fraction of H₂S produced by MSR being reoxidized; see supplementary section 5 for a full description of the model equations and parameters). The isotope fractionation factors are fixed for all processes except for MSR, for which the full ϵ_{MSR} and λ_{MSR} ranges have been explored (see supplementary section 4.2 for further explanation).

5.3.2. Cryptic sulfur cycling during the formation of VdG gypsum layers

The best fit of the model results to the analytical dataset (Figure 8) is obtained with $f_{msr} = 0.8$ (representing the fraction of sulfur entering the system as SO₄ and subsequently reduced by MSR, see Supplementary section 7), and scenario (iv), i.e. the partial oxidation of sulfide to elemental sulfur by chemolithotrophs and subsequent disproportionation of elemental sulfur (Figure 7.C and Figure 8). See Supplementary section 8 for further discussion on the reoxidative processes involved in sulfur cycling. In this best fit model run, 90% of the isotopic data in both diagrams ($\delta^{34}\text{S}_{\text{SO}_4} - \Delta^{33}\text{S}_{\text{SO}_4}$, Figure 8.A; $^{34}\epsilon_{\text{net}} - ^{33}\lambda_{\text{net}}$, Figure 8.B) plot within the area defined by $0.85 < f_{ox} < 1$. The combined sulfate and sulfide isotope dataset can therefore only be reproduced by considering that: (1) at least 80% of the net incoming sulfate is reduced microbially to H₂S rather than directly precipitated as gypsum ($f_{msr} > 0.8$) (Fig. 8), and (2) nearly all of the MSR-produced H₂S is reoxidized ($0.85 < f_{ox} < 1$) (Figure 8.). We suggest that the relatively high ϵ_{MSR} and f_{ox} values inferred for gypsum compared to lower values for marls indicates the occurrence of alternations between drastically different biogeochemical environments associated with periods of marl and gypsum deposition (Figure 7 and 8.).

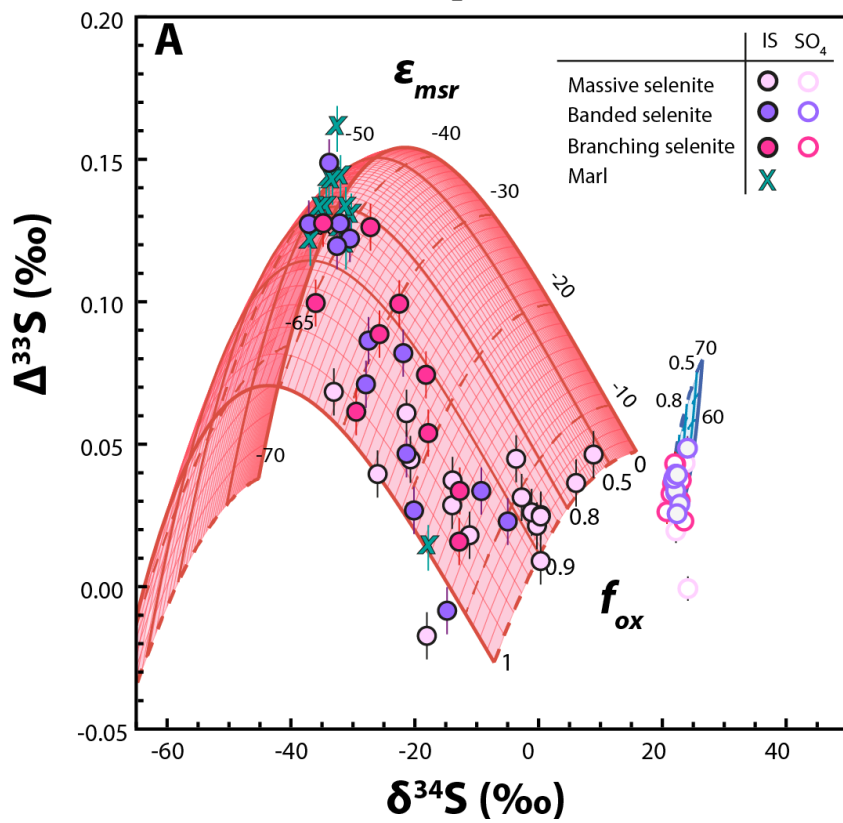
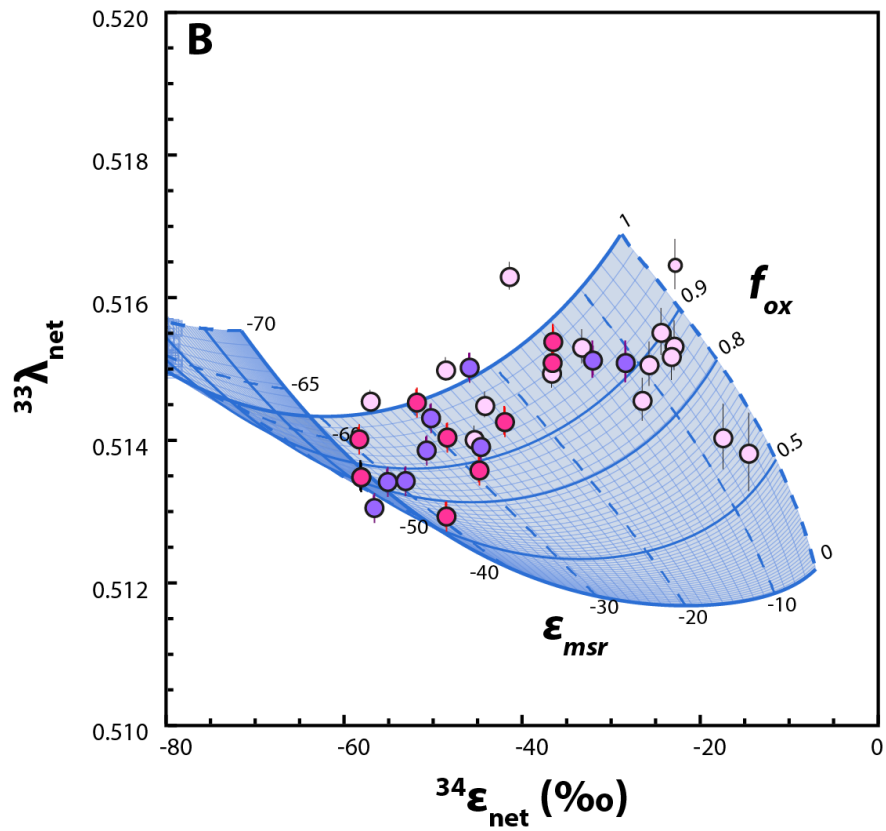


Figure 8. **Modelled isotope composition of VdG deposits compared to measured values.** Data points in **(A)** represent the $\Delta^{33}\text{S}$ vs $\delta^{34}\text{S}$ of sulfate and sulfide of gypsum (massive, banded, and branching selenite) and marl samples from the PLG unit of the VdG Basin. Data points in **(B)** represent the isotopic fractionation calculated for paired sulfate and sulfide in the various gypsum lithofacies (massive, banded, and branching selenite). Individual curves represent the modelled isotopic compositions in **(A)** and net fractionations factors in **(B)** for different values of f_{ox} (solid lines) and ϵ_{MSR} (dashed lines) the extent of isotopic fractionation during MSR. ϵ_{MSR} approaches -70‰ when thermodynamic equilibrium is reached and $f_{\text{ox}}=1$, indicating that all the sulfide produced by MSR is reoxidized. Note that in both diagrams most of the data fall in the area defined by $f_{\text{ox}}>0.85$, indicating the occurrence of nearly complete reoxidation of sulfide, and supports the occurrence of ongoing cryptic sulfur cycling during gypsum formation. Most of the data fall in the area defined by $\epsilon_{\text{MSR}}<-50$ ‰, indicating isotopic fractionation that deviated from thermodynamic equilibrium. (Error bars are 1σ).

These biogeochemical changes were controlled by orbitally driven climatic oscillations triggering changes in hydrological regime. During marl deposition (i.e. precession minima), freshwater inputs were higher, leading to water column stratification, less re-oxidation of hydrogen sulfide and an efficient preservation of organic matter (Natalicchio et al., 2019; Sabino et al., 2021) (Figure 1A and 7.A). Conversely, during gypsum precipitation (precession maxima), intense reoxidation of hydrogen sulfide prevailed (Figure 1B and 7B), requiring at least seasonal mixing of the water column. The large majority of sulfur (>80%) forming gypsum was first reduced from sulfate to sulfide by MSR, possibly stored as elemental sulfur and then almost completely reoxidized back to sulfate (>85%) resulting in low net production of H_2S (Figure 7B,C) and confirming the existence of a “cryptic” sulfur cycle during gypsum formation.

6. Implications for carbon cycling and gypsum formation

To our knowledge, this is the first time that gypsum deposits are proven to be formed from sulfate sourced almost entirely from cryptic sulfur cycling. The average rate of vertical gypsum accumulation at VdG was $1.4 \text{ mm}\cdot\text{year}^{-1}$ (Reghizzi et al., 2018). Given that our model results imply that more than 80% of sulfate constituting this gypsum was first reduced by MSR, we calculated that approximately $1.9 \text{ mmol}\cdot\text{cm}^{-2}\cdot\text{year}^{-1}$ of sulfate was consumed by MSR. Then, by considering a rough C:S stoichiometry of 2:1 for the MSR reaction (Jørgensen, 2021), we estimated a gross benthic organic carbon flux of $3.8 \text{ mmol}\cdot\text{cm}^{-2}\cdot\text{year}^{-1}$ remineralized by MSR during PLG gypsum formation. This is consistent with the large amounts of organic matter contained in the VdG interbeds. Marl deposits have a total organic carbon (TOC) content comparable to that of euxinic

environments (Jovovic et al., 2020; Lugli et al., 2007; Sinninghe Damsté et al., 1995), whilst TOC concentrations in gypsum range between 0.1 to 0.96% (Lugli et al., 2007), which is substantial considering the enormous dilution effect arising from gypsum depositional rates that are 25 to 250 times greater than marls (Reghizzi et al., 2018)). The benthic carbon flux involved in MSR we estimate for the VdG basin is comparable to that occurring in the world's most productive ocean regions, such as the Benguela and Peru-Chile margins, where the organic carbon remineralized through MSR ranges between 0.2 and 20mmol.cm⁻².yrs⁻¹ (Bowles et al., 2014; Treude et al., 2021). In these areas, dense mats populated by microbial sulfate reducers and CSB, similar to the fossil microbial assemblages found in the VdG gypsum, fuel a cryptic sulfur cycle (Brüchert et al., 2006; Callbeck et al., 2021; Treude et al., 2021).

The above considerations do not necessarily imply that the VdG basin was characterized by similar primary productivity to modern oxygen minimum zones but, rather, by comparable benthic carbon fluxes and carbon and sulfur cycling rates. Indeed, aerobic consumption of organic carbon in the VdG basin may have been limited to the upper layer of the water column due to density stratification (Natalicchio et al., 2022), leading to high organic carbon export fluxes (Pellegrino et al., 2021) and large quantities of benthic organic carbon available for MSR (Figure 7.). Conversely, very high primary productivity controls the export flux of organic carbon in modern productive margins.

Our findings support a recent model of PLG deposition (Aloisi et al., 2022) which suggests that the activity of benthic CSB mats drove increases in dissolved sulfate concentration and triggering gypsum precipitation. The inhibition of gypsum precipitation in deeper, more distal lateral equivalents of PLG gypsum (Natalicchio et al., 2019; Sabino et al., 2021), together with our results showing that more than 80% of the sulfate constituting the more marginal VdG gypsum has been cycled through a dynamic sulfur cycle, suggest that gypsum precipitation could have been controlled by the efficiency of the re-oxidative portion of the sulfur cycle, i.e. the cryptic cycling of sulfur.

7. Concluding remarks

Our work suggests a tight coupling of microbially driven sulfate reduction and sulfide oxidation in the Vena del Gesso basin.

Primary Lower Gypsum deposits accumulated during the first phase of the Messinian Salinity Crisis and characterized by identical lithofacies, stacking patterns, petrographic features and microbial fossils are widespread across the Mediterranean (see Figure 1.C) (Lugli et al., 2010; Natalicchio et al., 2022; Pellegrino et al., 2021). Whereas these deposits were previously thought

to be restricted to semi-enclosed basins with a water column depth of no more than 200m (Lugli et al., 2010), recent studies have demonstrated that some were deposited at depths of up to 800m and in basins not necessarily restricted by a sill (Ochoa et al., 2015; Raad et al., 2021).

If the cryptic sulfur cycle we describe was also active during the deposition of gypsum elsewhere in the Mediterranean, this would imply that the restriction of the Atlantic connection at the end of the Miocene led to not only the widespread deposition of evaporites, but also the significantly altered the short-term carbon and sulfur cycles of the Mediterranean (Waldeck et al., 2022). Further, the extensive occurrence of microbial mats populated by CSB on modern high-productivity continental margins or restricted basins, together with the results of the present study, suggest that cryptic sulfur cycling might have been prevalent in analogue evaporitic environments of the geological past.

Bibliography

- Aller, R.C., Madrid, V., Chistoserdov, A., Aller, J.Y. and Heilbrun, C. (2010) Unsteady diagenetic processes and sulfur biogeochemistry in tropical deltaic muds: Implications for oceanic isotope cycles and the sedimentary record. *Geochimica et Cosmochimica Acta* 74, 4671-4692.
- Aloisi, G., Guibourdenche, L., Natalicchio, M., Caruso, A., Haffert, L., El Kilany, A. and Dela Pierre, F. (2022) The geochemical riddle of “low-salinity gypsum” deposits. *Geochimica et Cosmochimica Acta*.
- Bak, F. and Cypionka, H. (1987) A novel type of energy metabolism involving fermentation of inorganic sulphur compounds. *Nature* 326, 891-892.
- Balci, N., Shanks III, W.C., Mayer, B. and Mandernack, K.W. (2007) Oxygen and sulfur isotope systematics of sulfate produced by bacterial and abiotic oxidation of pyrite. *Geochimica et Cosmochimica Acta* 71, 3796-3811.
- Blonder, B., Boyko, V., Turchyn, A.V., Antler, G., Sinichkin, U., Knossow, N., Klein, R. and Kamyshny, A. (2017) Impact of Aeolian Dry Deposition of Reactive Iron Minerals on Sulfur Cycling in Sediments of the Gulf of Aqaba. *Frontiers in Microbiology* 8.
- Boschetti, T., Cortecchi, G., Toscani, L. and Iacumin, P. (2011) Sulfur and oxygen isotope compositions of Upper Triassic sulfates from Northern Apennines (Italy): palaeogeographic and hydrogeochemical implications. *Geologica Acta*, 129-147.
- Bowles, M.W., Mogollón, J.M., Kasten, S., Zabel, M. and Hinrichs, K.-U. (2014) Global rates of marine sulfate reduction and implications for sub-sea-floor metabolic activities. *Science* 344, 889.
- Bradley, A.S., Leavitt, W.D., Schmidt, M., Knoll, A.H., Girguis, P.R. and Johnston, D.T. (2016) Patterns of sulfur isotope fractionation during microbial sulfate reduction. *Geobiology* 14, 91-101.
- Bradley, J., Arndt, S., Amend, J., Burwicz, E., Dale, A.W., Egger, M. and LaRowe, D.E. (2020) Widespread energy limitation to life in global seafloor sediments. *Science advances* 6, eaba0697.

Brüchert, V., Currie, B., Peard, K., Lass, H., Endler, R., Dübecke, A., Julies, E., Leipe, T. and Zitzmann, S. (2006) "Biogeochemical and physical control on shelf anoxia and water column hydrogen sulphide in the Benguela coastal upwelling system off Namibia," pp. 161-193.

Brüchert, V., Knoblauch, C. and Jørgensen, B.B. (2001) Controls on stable sulfur isotope fractionation during bacterial sulfate reduction in Arctic sediments. *Geochimica et Cosmochimica Acta* 65, 763-776.

Brunner, B., Bernasconi, S.M., Kleikemper, J. and Schroth, M.H. (2005) A model for oxygen and sulfur isotope fractionation in sulfate during bacterial sulfate reduction processes. *Geochimica et Cosmochimica Acta* 69, 4773-4785.

Bulian, F., Sierro, F.J., Ledesma, S., Jiménez-Espejo, F.J. and Bassetti, M.-A. (2021) Messinian West Alboran Sea record in the proximity of Gibraltar: Early signs of Atlantic-Mediterranean gateway restriction. *Marine Geology* 434, 106430.

Burke, A., Present, T.M., Paris, G., Rae, E.C.M., Sandilands, B.H., Gaillardet, J., Peucker-Ehrenbrink, B., Fischer, W.W., McClelland, J.W., Spencer, R.G.M., Voss, B.M. and Adkins, J.F. (2018) Sulfur isotopes in rivers: Insights into global weathering budgets, pyrite oxidation, and the modern sulfur cycle. *Earth and Planetary Science Letters* 496, 168-177.

Callbeck, C.M., Canfield, D.E., Kuypers, M.M.M., Yilmaz, P., Lavik, G., Thamdrup, B., Schubert, C.J. and Bristow, L.A. (2021) Sulfur cycling in oceanic oxygen minimum zones. *Limnology and Oceanography* n/a.

Canfield, D.E., Kristensen, E. and Thamdrup, B. (2005) Aquatic geomicrobiology. *Cita*, M. and Ryan, W. (1978) Messinian paleoenvironments.

Claypool, G.E., Holser, W.T., Kaplan, I.R., Sakai, H. and Zak, I. (1980) The age curves of sulfur and oxygen isotopes in marine sulfate and their mutual interpretation. *Chemical Geology* 28, 199-260.

Colangelo-Lillis, J., Pelikan, C., Herbold, C.W., Altshuler, I., Loy, A., Whyte, L.G. and Wing, B.A. (2019) Diversity decoupled from sulfur isotope fractionation in a sulfate-reducing microbial community. *Geobiology* 17, 660-675.

Crockford, P.W., Kunzmann, M., Bekker, A., Hayles, J., Bao, H., Halverson, G.P., Peng, Y., Bui, T.H., Cox, G.M., Gibson, T.M., Wörndle, S., Rainbird, R., Lepland, A., Swanson-Hysell, N.L., Master, S., Sreenivas, B., Kuznetsov, A., Krupenik, V. and Wing, B.A. (2019) Claypool continued: Extending the isotopic record of sedimentary sulfate. *Chemical Geology* 513, 200-225.

Damsté, S.J.S., Frewin, N.L., Kenig, F. and De Leeuw, J.W. (1995) Molecular indicators for palaeoenvironmental change in a Messinian evaporitic sequence (Vena del Gesso, Italy). I: Variations in extractable organic matter of ten cyclically deposited marl beds. *Organic Geochemistry* 23, 471-483.

Dela Pierre, F., Clari, P., Natalicchio, M., Ferrando, S., Giustetto, R., Lozar, F., Lugli, S., Manzi, V., Roveri, M. and Violanti, D. (2014) Flocculent layers and bacterial mats in the mudstone interbeds of the Primary Lower Gypsum unit (Tertiary Piedmont basin, NW Italy): Archives of palaeoenvironmental changes during the Messinian salinity crisis. *Marine Geology* 355, 71-87.

Dela Pierre, F., Natalicchio, M., Ferrando, S., Giustetto, R., Birgel, D., Carnevale, G., Gier, S., Lozar, F., Marabello, D. and Peckmann, J. (2015) Are the large filamentous microfossils preserved in Messinian gypsum colorless sulfide-oxidizing bacteria? *Geology* 43, 855-858.

El Kilany, A. (2018) Hydrologie et cycles biogéochimiques du soufre dans deux bassins marginaux de Méditerranée pendant la Crise de Salinité Messinienne, LOCEAN - Laboratoire

d'Océanographie et du Climat : Expérimentations et Approches Numériques Université Sorbonne Paris Cité p. 274.

Eldridge, D.L., Guo, W. and Farquhar, J. (2016) Theoretical estimates of equilibrium sulfur isotope effects in aqueous sulfur systems: Highlighting the role of isomers in the sulfite and sulfoxylate systems. *Geochimica et Cosmochimica Acta* 195, 171-200.

Evans, N.P., Turchyn, A.V., Gázquez, F., Bontognali, T.R., Chapman, H.J. and Hodell, D.A. (2015) Coupled measurements of $\delta^{18}\text{O}$ and δD of hydration water and salinity of fluid inclusions in gypsum from the Messinian Yesares Member, Sorbas Basin (SE Spain). *Earth and Planetary Science Letters* 430, 499-510.

Fike, D.A., Bradley, A.S. and Rose, C.V. (2015) Rethinking the ancient sulfur cycle. *Annual Review of Earth and Planetary Sciences* 43, 593-622.

Fike, D.A., Gammon, C.L., Ziebis, W. and Orphan, V.J. (2008) Micron-scale mapping of sulfur cycling across the oxycline of a cyanobacterial mat: a paired nanoSIMS and CARD-FISH approach. *The ISME Journal* 2, 749-759.

Fotherby, A., Bradbury, H.J., Antler, G., Sun, X., Druhan, J.L. and Turchyn, A.V. (2021) Modelling the Effects of Non-Steady State Transport Dynamics on the Sulfur and Oxygen Isotope Composition of Sulfate in Sedimentary Pore Fluids. *Frontiers in Earth Science* 8.

García-Veigas, J., Cendón, D.I., Gibert, L., Lowenstein, T.K. and Artiaga, D. (2018) Geochemical indicators in Western Mediterranean Messinian evaporites: Implications for the salinity crisis. *Marine Geology* 403, 197-214.

Gilhooly, W.P., Reinhard, C.T. and Lyons, T.W. (2016) A comprehensive sulfur and oxygen isotope study of sulfur cycling in a shallow, hyper-euxinic meromictic lake. *Geochimica et Cosmochimica Acta* 189, 1-23.

Gomes, M.L. and Hurtgen, M.T. (2015) Sulfur isotope fractionation in modern euxinic systems: Implications for paleoenvironmental reconstructions of paired sulfate–sulfide isotope records. *Geochimica et Cosmochimica Acta* 157, 39-55.

Halevy, I., Peters, S.E. and Fischer, W.W. (2012) Sulfate Burial Constraints on the Phanerozoic Sulfur Cycle. *Science* 337, 331-334.

Hsü, K.J., Ryan, W.B.F. and Cita, M.B. (1973) Late Miocene Desiccation of the Mediterranean. *Nature* 242, 240-244.

Isaji, Y., Kawahata, H., Takano, Y., Ogawa, N.O., Kuroda, J., Yoshimura, T., Lugli, S., Manzi, V., Roveri, M. and Ohkouchi, N. (2019) Diazotrophy Drives Primary Production in the Organic-Rich Shales Deposited Under a Stratified Environment During the Messinian Salinity Crisis (Vena del Gesso, Italy). *Frontiers in Earth Science* 7.

Johnston, D.T., Farquhar, J., Habicht, K.S. and Canfield, D.E. (2008) Sulphur isotopes and the search for life: strategies for identifying sulphur metabolisms in the rock record and beyond. *Geobiology* 6, 425-435.

Jørgensen, B.B. (2021) SULFUR BIOGEOCHEMICAL CYCLE OF MARINE SEDIMENTS. *Geochemical Perspectives* 10, 145-146.

Jovovic, I., Grossi, V., Adam, P., Simon, L., Antheaume, I., Gelin, F., Ader, M. and Cartigny, P. (2020) Quantitative and specific recovery of natural organic and mineral sulfur for (multi-)isotope analysis. *Organic Geochemistry* 146, 104055.

Kah, L.C., Lyons, T.W. and Chesley, J.T. (2001) Geochemistry of a 1.2 Ga carbonate-evaporite succession, northern Baffin and Bylot Islands: implications for Mesoproterozoic marine evolution. *Precambrian Research* 111, 203-234.

Kouwenhoven, T.J., Morigi, C., Negri, A., Giunta, S., Krijgsman, W. and Rouchy, J.M. (2006) Paleoenvironmental evolution of the eastern Mediterranean during the Messinian:

Constraints from integrated microfossil data of the Pissouri Basin (Cyprus). *Marine Micropaleontology* 60, 17-44.

Krijgsman, W., Hilgen, F.J., Raffi, I., Sierro, F.J. and Wilson, D.S. (1999) Chronology, causes and progression of the Messinian salinity crisis. *Nature* 400, 652-655.

Laskar, J., Fienga, A., Gastineau, M. and Manche, H. (2011) La2010: a new orbital solution for the long-term motion of the Earth. *Astronomy & Astrophysics* 532, A89.

Lugli, S., Bassetti, M.A., Manzi, V., Barbieri, M., Longinelli, A., Roveri, M., Schreiber, B.C., Lugli, S. and Babel, M. (2007) The Messinian 'Vena del Gesso' evaporites revisited: characterization of isotopic composition and organic matter, *Evaporites Through Space and Time*. Geological Society of London, p. 0.

Lugli, S., Manzi, V., Roveri, M. and Schreiber, B.C. (2010) The Primary Lower Gypsum in the Mediterranean: a new facies interpretation for the first stage of the Messinian salinity crisis. *Palaeogeography, Palaeoclimatology, Palaeoecology* 297, 83-99.

Mancini, A., Grelaud, M., Ziveri, P., Nallino, E. and Lozar, F. (2021) Calcareous Nannofossil Size and Abundance Response to the Messinian Salinity Crisis Onset and Paleoenvironmental Dynamics. *Paleoceanography and Paleoclimatology*.

Markovic, S., Paytan, A., Li, H. and Wortmann, U.G. (2016) A revised seawater sulfate oxygen isotope record for the last 4Myr. *Geochimica et Cosmochimica Acta* 175, 239-251.

Masterson, A., Alperin, M.J., Berelson, W.M. and Johnston, D.T. (2018) Interpreting multiple sulfur isotope signals in modern anoxic sediments using a full diagenetic model (California-Mexico margin: Alfonso Basin). *American Journal of Science* 318, 459-490.

Masterson, A.L., Wing, B.A., Paytan, A., Farquhar, J. and Johnston, D.T. (2016) The minor sulfur isotope composition of Cretaceous and Cenozoic seawater sulfate. *Paleoceanography* 31, 779-788.

Melegy, A. and Ismael, I. (2013) Microstructure and geochemistry studies on Messinian gypsum deposits from the Northern Coast of Egypt. *Arabian Journal of Geosciences* 7.

Natalicchio, M., Birgel, D., Dela Pierre, F., Ziegenbalg, S., Hoffmann-Sell, L., Gier, S. and Peckmann, J. (2022) Messinian bottom-grown selenitic gypsum: An archive of microbial life. *Geobiology*.

Natalicchio, M., Dela Pierre, F., Birgel, D., Brumsack, H., Carnevale, G., Gennari, R., Gier, S., Lozar, F., Pellegrino, L., Sabino, M., Schnetger, B. and Peckmann, J. (2019) Paleoenvironmental change in a precession-paced succession across the onset of the Messinian salinity crisis: Insight from element geochemistry and molecular fossils. *Palaeogeography, Palaeoclimatology, Palaeoecology* 518, 45-61.

Ochoa, D., Sierro, F.J., Lofi, J., Maillard, A., Flores, J.-A. and Suárez, M. (2015) Synchronous onset of the Messinian evaporite precipitation: First Mediterranean offshore evidence. *Earth and Planetary Science Letters* 427, 112-124.

Ono, S., Wing, B., Johnston, D., Farquhar, J. and Rumble, D. (2006) Mass-dependent fractionation of quadruple stable sulfur isotope system as a new tracer of sulfur biogeochemical cycles. *Geochimica et Cosmochimica Acta* 70, 2238-2252.

Ortí, F., Rosell, L. and Anadón, P. (2010) Diagenetic gypsum related to sulfur deposits in evaporites (Libros Gypsum, Miocene, NE Spain). *Sedimentary Geology* 228, 304-318.

Panieri, G., Lugli, S., Manzi, V., Palinska, K.A. and Roveri, M. (2008) Microbial communities in Messinian evaporite deposits of the Vena del Gesso (northern Apennines, Italy). *Stratigraphy* 5, 343-352.

Pasquier, V., Bryant, R.N., Fike, D.A. and Halevy, I. (2021a) Strong local, not global, controls on marine pyrite sulfur isotopes. *Science Advances* 7, eabb7403.

Pasquier, V., Fike, D.A. and Halevy, I. (2021b) Sedimentary pyrite sulfur isotopes track the local dynamics of the Peruvian oxygen minimum zone. *Nature Communications* 12, 4403.

Pasquier, V., Sansjofre, P., Rabineau, M., Revillon, S., Houghton, J. and Fike, D.A. (2017) Pyrite sulfur isotopes reveal glacial– interglacial environmental changes. *Proceedings of the National Academy of Sciences* 114, 5941-5945.

Pellegrino, L., Natalicchio, M., Abe, K., Jordan, R., Longo, S., Ferrando, S., Carnevale, G. and Dela Pierre, F. (2021) Tiny, glassy, and rapidly trapped: The nano-sized planktic diatoms in Messinian (late Miocene) gypsum. *Geology* 49.

Pellerin, A., Bui, T.H., Rough, M., Mucci, A., Canfield, D.E. and Wing, B.A. (2015) Mass-dependent sulfur isotope fractionation during reoxidative sulfur cycling: A case study from Mangrove Lake, Bermuda. *Geochimica et Cosmochimica Acta* 149, 152-164.

Pierre, C. (1982) Teneurs en isotopes stables (^{18}O , ^2H , ^{13}C , ^{34}S) et conditions de g n se des  vaporites marines: application   quelques milieux actuels et au Messinien de la M diterran e.  diteur inconnu.

Raad, F., Lofi, J., Maillard, A., Tzevahirtzian, A. and Caruso, A. (2021) The Messinian Salinity Crisis deposits in the Balearic Promontory: An undeformed analog of the MSC Sicilian basins?? *Marine and Petroleum Geology* 124, 104777.

Reghizzi, M., Lugli, S., Manzi, V., Rossi, F.P. and Roveri, M. (2018) Orbitally Forced Hydrological Balance During the Messinian Salinity Crisis: Insights From Strontium Isotopes ($^{87}\text{Sr}/^{86}\text{Sr}$) in the Vena del Gesso Basin (Northern Apennines, Italy). *Paleoceanography and Paleoclimatology* 33, 716-731.

Roveri, M., Flecker, R., Krijgsman, W., Lofi, J., Lugli, S., Manzi, V., Sierro, F.J., Bertini, A., Camerlenghi, A. and De Lange, G. (2014) The Messinian Salinity Crisis: past and future of a great challenge for marine sciences. *Marine Geology* 352, 25-58.

Sabino, M., Dela Pierre, F., Natalicchio, M., Birgel, D., Gier, S. and Peckmann, J. (2021) The response of water column and sedimentary environments to the advent of the Messinian salinity crisis: insights from an onshore deep-water section (Govone, NW Italy). *Geological Magazine*.

Sabino, M., Schefu , E., Natalicchio, M., Dela Pierre, F., Birgel, D., Bortels, D., Schnetger, B. and Peckmann, J. (2020) Climatic and hydrologic variability in the northern Mediterranean across the onset of the Messinian salinity crisis. *Palaeogeography, Palaeoclimatology, Palaeoecology* 545, 109632.

Sakai, H. (1971) Sulfur and oxygen isotopic study of barite concretions from banks in the Japan Sea off the Northeast Honshu, Japan. *GEOCHEMICAL JOURNAL* 5, 79-93.

Schopf, J.W., Farmer, J.D., Foster, I.S., Kudryavtsev, A.B., Gallardo, V.A. and Espinoza, C. (2012) Gypsum-permineralized microfossils and their relevance to the search for life on Mars. *Astrobiology* 12, 619-633.

Shields, G.A. and Mills, B.J.W. (2020) Evaporite weathering and deposition as a long-term climate forcing mechanism. *Geology* 49, 299-303.

Sim, M.S., Bosak, T. and Ono, S. (2011a) Large sulfur isotope fractionation does not require disproportionation. *Science* 333, 74-77.

Sim, M.S., Ono, S., Donovan, K., Templer, S.P. and Bosak, T. (2011b) Effect of electron donors on the fractionation of sulfur isotopes by a marine *Desulfovibrio* sp. *Geochimica et Cosmochimica Acta* 75, 4244-4259.

Sinninghe Damst , J.S., Frewin, N.L., Kenig, F. and De Leeuw, J.W. (1995) Molecular indicators for palaeoenvironmental change in a Messinian evaporitic sequence (Vena del

Gesso, Italy). I: Variations in extractable organic matter of ten cyclically deposited marl beds. *Organic Geochemistry* 23, 471-483.

Stam, M.C., Mason, P.R.D., Laverman, A., Pallud, C. and Van Cappellen, P. (2006) $^{34}\text{S}/^{32}\text{S}$ fractionation by sulfate-reducing microbial communities in estuarine sediments. *Geochimica et Cosmochimica Acta* 70.

Thamdrup, B., Finster, K., Hansen, J.W. and Bak, F. (1993) Bacterial Disproportionation of Elemental Sulfur Coupled to Chemical Reduction of Iron or Manganese. *Applied and Environmental Microbiology* 59, 101-108.

Topper, R., Lugli, S., Manzi, V., Roveri, M. and Meijer, P. (2014) Precessional control of Sr ratios in marginal basins during the Messinian Salinity Crisis. *Geochemistry, Geophysics, Geosystems*.

Topper, R.P.M., Flecker, R., Meijer, P.T. and Wortel, M.J.R. (2011) A box model of the Late Miocene Mediterranean Sea: Implications from combined $^{87}\text{Sr}/^{86}\text{Sr}$ and salinity data. *Paleoceanography* 26.

Topper, R.P.M. and Meijer, P.T. (2015) The precessional phase lag of Messinian gypsum deposition in Mediterranean marginal basins. *Palaeogeography, Palaeoclimatology, Palaeoecology* 417, 6-16.

Tostevin, R., Turchyn, A.V., Farquhar, J., Johnston, D.T., Eldridge, D.L., Bishop, J.K.B. and McIlvin, M. (2014) Multiple sulfur isotope constraints on the modern sulfur cycle. *Earth and Planetary Science Letters* 396, 14-21.

Treude, T., Hamdan, L.J., Lemieux, S., Dale, A.W. and Sommer, S. (2021) Rapid sulfur cycling in sediments from the Peruvian oxygen minimum zone featuring simultaneous sulfate reduction and sulfide oxidation. *Limnology and Oceanography* n/a.

Utrilla, R., Pierre, C., Orti, F. and Pueyo, J.J. (1992) Oxygen and sulphur isotope compositions as indicators of the origin of Mesozoic and Cenozoic evaporites from Spain. *Chemical Geology* 102, 229-244.

Waldeck, A.R., Olson, H.C., Yao, W., Blättler, C.L., Paytan, A., Hodell, D.A. and Johnston, D.T. (2022) Calibrating the triple oxygen isotope composition of evaporite minerals as a proxy for marine sulfate. *Earth and Planetary Science Letters* 578, 117320.

Wing, B.A. and Halevy, I. (2014) Intracellular metabolite levels shape sulfur isotope fractionation during microbial sulfate respiration. *Proceedings of the National Academy of Sciences of the United States of America* 111, 18116-18125.

Zhang, G., Zhang, X., Hu, D., Li, D., Algeo, T.J., Farquhar, J., Henderson, C.M., Qin, L., Shen, M., Shen, D., Schoepfer, S.D., Chen, K. and Shen, Y. (2017) Redox chemistry changes in the Panthalassic Ocean linked to the end-Permian mass extinction and delayed Early Triassic biotic recovery. *Proc Natl Acad Sci U S A* 114, 1806-1810.

Supplementary Material

1. Isotopic measurements

1.1 Multiple sulfur isotopes

Sulfate from gypsum and chromium reducible sulfides (iron sulfide) from gypsum and marls were reduced into H₂S using two different reducing solutions following Jovovic et al. (2020). Released H₂S was trapped in a NaOH solution as HS⁻, transformed into Ag₂S by adding a AgNO₃ solution, purified with 3-5 drops of 68% HNO₃ to dissolve co-precipitating Ag₂O impurities (Geng et al., 2018), rinsed three times with Milli-Q H₂O and finally dried in an oven at 60°C. Ag₂S powder was then reacted in Ni-reaction bombs with F₂ at 250°C overnight to produce gaseous SF₆ that was purified cryogenically and by gas chromatography before to be analyzed by a dual inlet mass spectrometer MAT-253 at Institut de Physique du Globe de Paris (Geng et al., 2018; Ono et al., 2006). The $\delta^{34}\text{S}$ values were calibrated with an in-house SF₆ standard using IAEA-S1 international standard that have a value of -0.3‰ VS-CDT. Long term reproducibility of IAEA-S1 (n=7) yielded $\delta^{34}\text{S} = -0.30 \pm 0.2\text{‰}$ and $\Delta^{33}\text{S} = 0.081 \pm 0.004$. Error bars (1 σ) on the whole procedure for sulfate and sulfide extraction and measurements were respectively calculated from replicate extraction and analyses of internal barite (n=7) and marls (n=3) standards. We obtained 0.2 and 0.004‰ of error on $\delta^{34}\text{S}$ and $\Delta^{33}\text{S}$ of sulfate and 0.4 and 0.008‰ for $\delta^{34}\text{S}$ and $\Delta^{33}\text{S}$ respectively for sulfides.

1.2 Oxygen isotopes of sulfate

Oxygen isotope analyses of BaSO₄ (produced by re-precipitating the SO₄²⁻ ion of gypsum in a BaCl₂ solution) were conducted at University of Burgundy on a Elementar vario PYRO cube elemental analyzer in-line with an Isoprime 100 mass spectrometer in continuous flow mode; analytical errors are $\pm 0.4\text{‰}$ (2 σ) based on replicate analyses of the international barite standard

NBS-127. The $\delta^{18}\text{O}$ values were calibrated using the internal laboratory standard Edm-Tyr ($\delta^{18}\text{O} = +8.6 \text{ ‰ V-SMOW}$) that was calibrated against the IAEA international reference NBS 127 ($\delta^{18}\text{O} = +8.5 \pm 0.2 \text{ ‰ V-SMOW}$).

2. Data from the literature used in main text figures

2.1 Figure 1A and 2A

In Figure 1.a ,3 and 4 of the main text we use $\delta^{34}\text{S}$, $\Delta^{33}\text{S}$ and $\delta^{18}\text{O}$ from other studies. This includes:

- Estimate of the $\delta^{34}\text{S}$ and $\delta^{18}\text{O}$ isotopic composition of Messinian oceanic dissolved SO_4^{2-} (Markovic et al., 2016; Masterson et al., 2016; Turchyn and Schrag, 2004) (Fig. 1a and 3). The $\delta^{18}\text{O}_{\text{SO}_4}$ of the Messinian ocean is taken from (Turchyn and Schrag, 2004) and has a large error bar to account for the uncertainties pointed by (Markovic et al., 2016) linked to the measurement of $\delta^{18}\text{O}$ in barite samples from which the curve of $\delta^{18}\text{O}_{\text{SO}_4}$ through time originates (Fig. 3).
- $\delta^{34}\text{S}$ and $\delta^{18}\text{O}$ of PLG deposits from the Spanish marginal basins of Sorbas (Evans et al., 2015; García-Veigas et al., 2018), Bajo Segura (García-Veigas et al., 2018), Murcia (Pierre, 1982) and Mallorca (García-Veigas et al., 2018), the Italian marginal Piedmont (El Kilany, 2018) and Caltanissetta basins (El Kilany, 2018; García-Veigas et al., 2018) and the Polemi and Kalavassos/Psematismenos basins of Cyprus (Pierre, 1982) (Fig.3).
- $\delta^{34}\text{S}$ and $\delta^{18}\text{O}$ SO_4^{2-} isotopic composition range produced by pyrite oxidation (Balci et al., 2007; Burke et al., 2018) (Fig.3).
- Estimate of Mesozoic and Cenozoic evaporites SO_4^{2-} $\delta^{34}\text{S}$ and $\delta^{18}\text{O}$ isotopic composition (Boschetti et al., 2011 and references therein; Claypool et al., 1980; Crockford et al., 2019; Ortí et al., 2010; Sakai, 1971; Utrilla et al., 1992) (Fig.3).

- Modern sea water $\delta^{34}\text{S}$, $\Delta^{33}\text{S}$ and $\delta^{18}\text{O}$ SO_4^{2-} isotopic composition (Johnston et al., 2014)(Fig. 1a,3 and 4).

2.2 Figure 1.c

In figure 1.c, modified after Lofi (2018), the pink dots represent the PLG units that were correlated at the Mediterranean scale (Karakitsios et al., 2017; Krijgsman et al., 1999; Lugli et al., 2010; Orszag-Sperber et al., 2009). In addition, numerous gypsum deposits have been interpreted to correspond to Messinian gypsum in other basins of the Mediterranean, even though a precise tuning and dating have not been realized on these sections (see the orange dots and green dots in main text Fig 1.c). They consist of PLG and resedimented PLG i.e Resedimented Lower Gypsum or Upper Gypsum deposits (formed at the end of the Messinian Salinity Crisis). This includes gypsum drilled during DSDP/IODP oceanographic expeditions LEG 13, 42 and 107 (see the green dots in main text Fig 1.c) (Hsü et al., 1978a; Hsü et al., 1978b, c; Hsü et al., 1978d; Hsü et al., 1973; Kastens et al., 1987; Lugli et al., 2015) and gypsum from Albania (Pashko et al., 2019), Algeria (Rouchy et al., 2007), Adriatic foredeep (Manzi et al., 2020), Balearic Promontory (Ochoa et al., 2015; Raad et al., 2021), Calabria (Costanzo et al., 2019) in Italy, Cyprus (Robertson et al., 1995; Rouchy and Monty, 1981), Egypt (Aref, 2003; Melegy and Ismael, 2013), Israel (Cohen, 1993; Raab et al., 1997), Tunisia (El Euch-El Koundi et al., 2009; Harrab et al., 2013; Sghari, 2012), Turkey (Boulton et al., 2016; Tekin et al., 2010) and Syria (Hardenberg and Robertson, 2007; Rouchy et al., 2007).

2.3 Figure 5

In figure 5 of the main text we use data from laboratory experiments in order to compare them with the fractionation factors we calculated from our samples. Data from abiotic sulfide oxidation experiments comes from (Eldridge and Farquhar, 2018) (dark grey area with black dotted contour), data from pure cultures with sulfate reducers comes from (Bertran et al., 2018; Johnston et al., 2005; Leavitt et al., 2013; Sim et al., 2011a; and Sim et al., 2011b) (light grey

area) and data from pure culture experiments with disproportionators comes from (Johnston et al., 2005) (white area with grey dashed contour). White squares represent the $^{34}\epsilon_{\text{net}}$ and $^{33}\lambda_{\text{net}}$ measured in natural environments populated with biofilms dominated by chemolithotroph sulfide oxidizer (Magnuson et al., 2020; Zerkle et al., 2016).

2.4 Calibration of $\delta^{34}\text{S}$, $\Delta^{33}\text{S}$ and $\delta^{18}\text{O}$ sulfate isotopic data from this study and from the literature

$\delta^{34}\text{S}$ and $\delta^{18}\text{O}$ from this study have been set to the VSCDT and VSMOW scale respectively using recent calibration of NBS-127 reference material (Brand et al., 2014).

To compare these published data with ours, we corrected the reported data that were calibrated with obsolete values of NBS-127 by using the difference between the reported and newly calibrated $\delta^{34}\text{S}$ and $\delta^{18}\text{O}$ values of the standard following the method reported in Johnston et al. (2014). In addition, because there is a small and almost temperature-independent isotopic fractionation between the dissolved SO_4^{2-} ion and gypsum, we calculated the isotopic composition of the sulfate ion in equilibrium with gypsum by applying known fractionation factors (at earth surface temperature $\alpha^{34}_{\text{Gyp-SO}_4}=1.00165$ (Raab and Spiro, 1991; Thode and Monster, 1965; Van Driessche et al., 2016) ; $^{33}\alpha_{\text{Gyp-SO}_4}=1.00084$ and $\alpha^{18}_{\text{Gyp-SO}_4}=1.0035$ (Lloyd, 1968; Van Driessche et al., 2016)).

3. Isotopic data

3.1 Iron sulfide (IS) content and isotopic composition in gypsum and marls samples

Table S1: Concentrations and multiple sulfur isotopic composition of Iron sulfide from the Vena del Gesso gypsum and marly interbeds. Error is 1σ .

PLG Cycle	Facies	Sample name	$\Delta^{33}\text{S}_{\text{IS}}$ $\pm 0.008\text{‰}$	$\delta^{34}\text{S}_{\text{IS}}$ $\pm 0.4\text{‰}$	[IS] $\pm 100\text{ppm}$
1	Massive selenite	Ma I-01	0.045	-3.63	15
2	Massive selenite	Ma II-02	-0.017	-18.06	37
2	Massive selenite	Ma II-07	0.025	0.36	101
3	Marl	Pe III-01	0.143	-33.87	13317

3	Massive selenite	Ma III-01	0.046	8.88	111
4	Marl	Pe IV-01	0.132	-35.37	7614
4	Massive selenite	Ma IV-02	0.025	0.34	236
4	Banded selenite	Ba IV-05	0.120	-32.56	283
5	Marl	Pe V-01	0.142	-33.29	8791
5	Massive selenite	Ma V-03	0.018	-11.16	116
5	Banded selenite	Ba V-06	0.071	-27.89	225
6	Marl	Pe VI-01	0.161	-32.54	8590
6	Massive selenite	Ma VI-02	0.037	-13.90	76
6	Banded selenite	Ma VI-03	0.082	-21.86	251
6	Branching selenite	Br VI-04	0.034	-12.74	236
7	Marl	Pe VII-01	0.119	-31.12	1815
7	Laminated gypsum	La VII-02	0.120	-36.35	355
7	Massive selenite	Ma VII-03	0.068	-33.08	111
7	Banded selenite	Ba VII-04	0.034	-9.26	35
7	Branching selenite	Br VII-05	0.054	-17.83	97
7	Branching selenite	Ba VII-06	0.126	-27.16	351
8	Marl	Pe VIII-01	0.125	-32.08	1155
8	Massive selenite	Ma VIII-02	0.040	-26.00	240
8	Banded selenite	Ba VIII-03	0.086	-27.46	52
8	Branching selenite	Br VIII-04	0.089	-25.71	29
9	Marl	Pe IX-01	0.130	-30.26	2306
9	Massive selenite	Ma IX-02	0.061	-21.34	147
9	Banded selenite	Ba IX-03	0.122	-30.47	103
10	Marl	Pe X-01	0.132	-31.15	6190
10	Massive selenite	Ma X-02	0.045	-20.69	171
10	Banded selenite	Ba X-03	0.047	-21.33	145

10	Branching selenite	Br X-04	0.074	-18.19	148
11	Marl	Pe XI-01	0.143	-32.00	6362
11	Massive selenite	Ma XI-02	0.021	-0.26	191
11	Banded selenite	BA XI-03	0.149	-33.83	69
11	Branching selenite	Br XI-04	0.099	-22.51	270
12	Marl	Pe XII-03	0.133	-34.31	5543
12	Massive selenite	Ma XII-04	0.026	-1.11	240
12	Banded selenite	Ba XII-05	0.127	-32.09	112
12	Branching selenite	Br XII-06	0.128	-34.80	234
13	Banded selenite	Ba XIII-03	0.127	-37.12	502
13	Branching selenite	Br XIII-04	0.016	-12.84	166
14	Massive selenite	Ma XIV-02	0.036	6.06	117
14	Banded selenite	Ma XIV-03	0.023	-4.98	219
14	Branching selenite	Br XIV-04	0.061	-29.46	460
15	Marl	Pe XV-01	0.121	-36.86	2699
15	Massive selenite	Ma XV-02	0.029	-13.96	74
15	Banded selenite	Ba XV-03	-0.008	-14.78	80
15	Branching selenite	Br XV-04	0.100	-36.01	454
16	Marl	Pe XVI-01	0.014	-17.84	10197
16	Massive selenite	Ma XVI-02	0.031	-2.73	89
16	Massive selenite	Ma XVI-02 bis	0.009	0.34	98
16	Banded selenite	Ba XVI-05	0.027	-20.13	117

Iron sulfide concentrations calculated from our chromium reducible compound chemical extractions range from 15 to 502 ppm in selenite samples and from 1155 to 13117 ppm in marls (Table S1 and Fig. S1). The higher concentration of iron sulfide in marly interbeds are

comparable to sulfide concentration found in typical ancient and modern euxinic environments (Jovovic et al., 2020). Instead, sulfide concentrations in gypsum samples is much lower and variable.

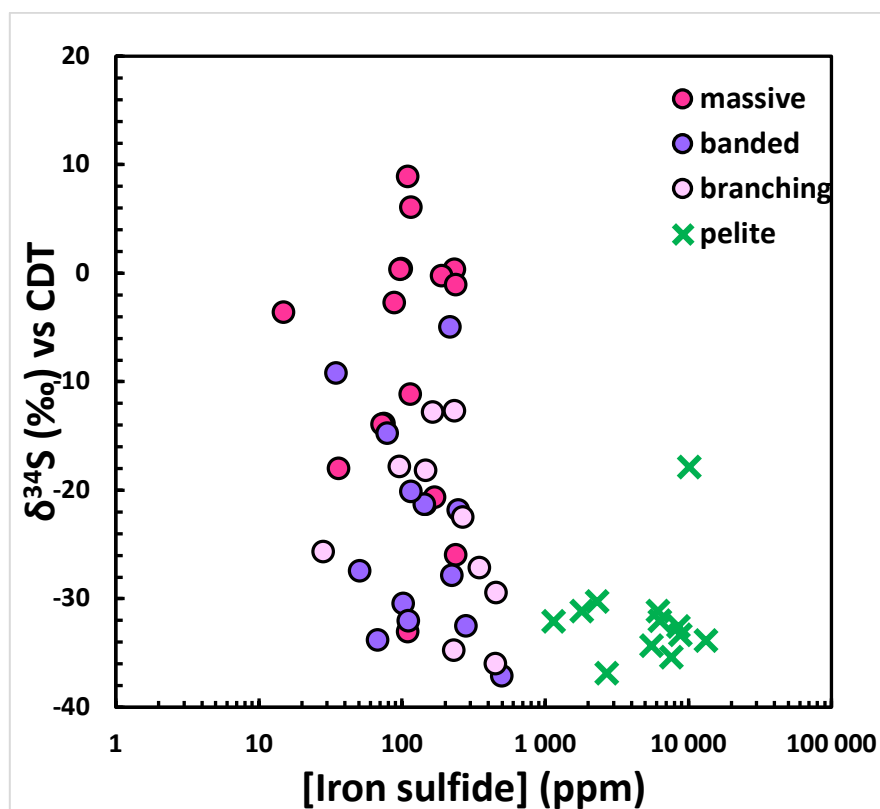


Figure S1: Concentration of sulfides within gypsum and marls interbeds of the Vena del Gesso succession as a function of their $\delta^{34}\text{S}_{\text{CRS}}$ isotopic composition

3.2 $\delta^{34}\text{S}$, $\delta^{18}\text{O}$ and $\Delta^{33}\text{S}$ isotopic compositions of sulfate from gypsum

Table S2: Oxygen and multiple sulfur isotope composition of dissolved sulfate ion from the Vena del Gesso gypsum. Error is 1σ .

Cycle	Facies	Sample name	$\Delta^{33}\text{S}_{\text{SO}_4}$ $\pm 0.004\text{‰}$	$\delta^{34}\text{S}_{\text{SO}_4}$ $\pm 0.2\text{‰}$	$\delta^{18}\text{O}_{\text{SO}_4}$ $\pm 0.2\text{‰}$
1	Massive selenite	Ma I-01	0.033	21.78	8.24
2	Massive selenite	MC II-02	0.037	22.65	9.26
2	Massive selenite	Ma II-07	0.033	22.10	n.d
3	Massive selenite	Ma III-01	0.029	22.06	8.67
4	Massive selenite	Ma IV-02	0.029	22.39	8.32

4	Banded selenite	MT IV-05	0.033	22.15	8.01
5	Massive selenite	Ma V-03	0.028	21.17	8.43
5	Banded selenite	Ba V-06	0.037	21.83	8.53
6	Massive selenite	Ma VI-02	0.036	21.92	9.24
6	Banded selenite	Ma VI-03	0.034	22.13	8.88
6	Branching selenite	Br VI-04	0.037	23.05	8.80
7	Laminar selenite	La VII-02	0.033	21.38	n.d
7	Massive selenite	Ma VII-03	0.043	23.68	n.d
7	Banded selenite	Ba VII-04	0.038	21.85	9.05
7	Branching selenite	Br VII-05	0.023	23.47	8.66
7	Branching selenite	Br VII-06	0.026	20.73	8.76
8	Massive selenite	Ma VIII-02	0.039	22.00	8.33
8	Banded selenite	Ba VIII-03	0.029	22.81	9.36
8	Branching selenite	Br VIII-04	0.043	22.15	9.01
9	Massive selenite	Ma IX-02	0.039	22.17	9.01
9	Banded selenite	Ba IX-03	0.040	22.19	9.66
10	Massive selenite	Ma X-02	-0.001	24.12	9.99
10	Banded selenite	Ba X-03	0.049	24.05	9.29
11	Banded selenite	Ba XI-03	0.039	22.44	9.81
11	Branching selenite	Br XI-04	0.036	21.64	9.39
12	Massive selenite	Ma XII-04	0.039	22.12	10.39
13	Branching selenite	Br XIII-04	0.030	22.87	10.08
14	Massive selenite	Ma XIV-02	0.020	22.18	10.09

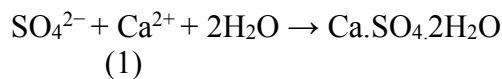
14	Banded selenite	Ba XIV-03	0.026	22.37	10.20
14	Branching selenite	Br XIV-04	0.038	21.89	10.08
15	Branching selenite	Br XV-04	0.043	21.99	10.11
16	Massive selenite	Ma XVI-02	0.033	21.88	n.d
16	Massive selenite	Ma XVI-02 bis	0.043	21.98	10.11

4. Biogeochemical processes and their fractionation factors

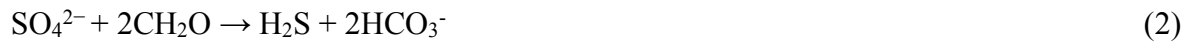
Sulfur isotope composition of gypsum and pyrite accumulating in a marginal basin can vary as a function of (i) mixing between the ocean- and river-derived sulfate sources, (ii) the magnitude of gypsum and pyrite burial fluxes and (iii) the extent and mode of intra-basinal biogeochemical sulfur cycling and the associated isotope fractionation.

Within the marginal basin, sulfur is abiotically and microbiologically partitioned between the three sulfur pools of SO_4^{2-} , S° and H_2S via the following processes:

I. gypsum accumulation with rate F_{gyp} that extracts sulfate from the marginal basin:



II. Dissimilatory microbial sulfate reduction (MSR) into sulfide, performed by sulfate reducing bacteria, with rate F_{msr} :

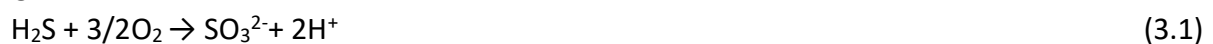


III. oxidation of sulfide produced by MSR to sulfate, with rate F_{ox} , which can take place:

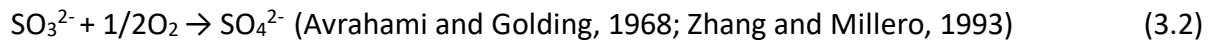
(iii.1) chemically, using molecular oxygen or metal oxides as electron acceptors



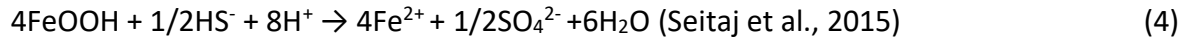
Or



and



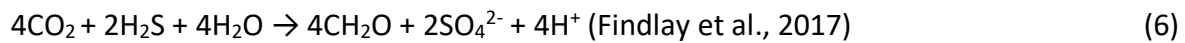
Or



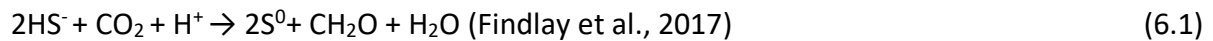
Or



(iii.2) biologically, via phototrophic sulfide oxidation (green or purple sulfur bacteria):



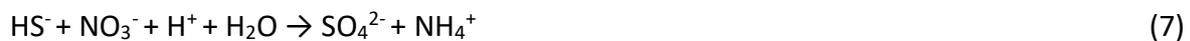
Or



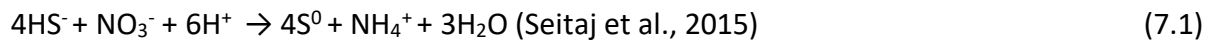
and



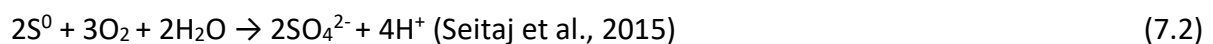
(iii.3) biologically, via chemolithotrophic sulfide oxidation (colorless sulfur bacteria) using O₂ or NO₃⁻ as electron acceptors:



Or



and



In our model, the oxidation of H₂S takes place *either* via processes 3,4,5,6 or 7 (with SO₄²⁻ as an end product) *or* via processes 3.1, 6.1 or 7.1 (with S⁰ or SO₃²⁻ as an end product). While the rate of all of these four processes is denoted **F_{ox}**, each of the four processes implies a distinct sulfur isotope fractionation, as defined in Table S3.

If not reoxidated into sulfate, the produced intermediate sulfur compound (S⁰ or SO₃²⁻) can be involved in:

IV. disproportionation of S⁰ or SO₃²⁻ producing sulfate and sulfide, with rates **F_{do} and **F_{dh}**, respectively:**

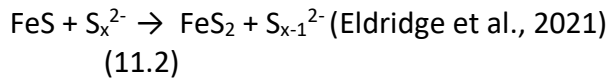
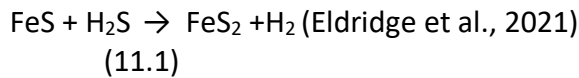
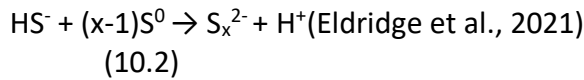
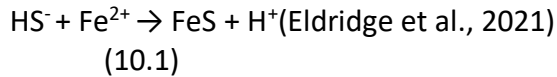


Or



Finally, aqueous sulfide produced by microbial reactions can be extracted from the sulfur cycling of marginal basins by

V. solid iron sulfide formation and burial (F_{crs}):



4.1 Fixed fractionation factors

Sulfur isotope fractionation takes place during the biogeochemical processes introduced above as well as gypsum and pyrite burial fluxes. Fractionation factors α and λ are assigned fixed values (see Table S3), except for MSR for which isotope fractionation is a function of the cellular rate of microbial sulfate reduction (see section 4.2). In table S3, R_x are the isotope ratios ($^{x}S/^{32}S$, where $x = 34$ or 33) of the sulfur fluxes involved in the fractionation processes: R_{oc} is the sulfur isotope ratio of the sulfate input from the ocean, R_{riv} is the sulfur isotope ratio of sulfate input from the rivers, R_{mb} is the sulfur isotope ratio of sulfate in the marginal basin, R_{gyp} is the sulfur isotope ratio of gypsum precipitated in the marginal basin, R_{msr} is the sulfur isotope ratio of H_2S produced by MSR, R_{ox} is the sulfur isotope ratio of S^0 produced by oxidation of H_2S , R_{do} is the sulfur isotope ratio of SO_4^{2-} produced by disproportionation of S^0 (or SO_3^{2-}) and R_{dh} is the sulfur isotope ratio of H_2S produced by disproportionation of S^0 .

Table S3: Sulfur fractionation factors used in the numerical model

Reaction	Process	$^{34}\alpha$	$^{33}\alpha$	$^{34}\epsilon$ (‰)	$^{33}\lambda$	Reference
<i>Gypsum precipitation</i> $\frac{{}^xR_{gyp}}{{}^xR_{mb}}$	Equation (1)	1,00165	1,00085	1,65	0,515	(Thode and Monster, 1965)
<i>Solid Sulfide Burial</i> $\frac{{}^xR_{py}}{{}^xR_{H2S}}$	Equations (10), (11.1) and (11.2)	1	1	0	0,515	(Eldridge et al., 2021; Fry et al., 1986)*
	Inorganic H ₂ S to SO ₄ ²⁻ Equations (3), (4) or (5)	0,99440	0,99715	-5,6	0,508	(Eldridge and Farquhar, 2018)*
<i>Sulfide Oxidation</i> $\frac{{}^xR_{ox}}{{}^xR_{H2S}}$	Phototrophic H ₂ S to SO ₄ ²⁻ Equation (6)	1,00154	1,00081	1,5	0,529	(Zerkle et al., 2009)
	Phototrophic H ₂ S to S ⁰ Equation (6.1)	1,00189	1,00099	1,89	0,535	(Zerkle et al., 2009)
	Chemolithotrophic H ₂ S to S ⁰ Equations (7.1)	0,99600	0,99795	4	0,513	(Zerkle et al., 2016)
	Phototrophic S ⁰ to SO ₄ ²⁻ Equation (6.2)	0,99810	0,99906	-1,9	0,495	(Zerkle et al., 2009)
<i>Intermediate compound Oxidation</i> $\frac{{}^xR_{do}}{{}^xR_{Si}}$	Disproportion S ⁰ to SO ₄ ²⁻ Equation (8)	1,01853	1,009584	18,5	0,519	(Johnston et al., 2007; Johnston et al., 2005)
	Disproportion SO ₃ ²⁻ to SO ₄ ²⁻ Equation (9)	1,01000	1,00527	10	0,528	(Johnston et al., 2005; Pellerin et al., 2015)*
<i>Intermediate Compound Reduction</i> $\frac{{}^xR_{dh}}{{}^xR_{Si}}$	Disproportion S ⁰ to H ₂ S Equation (8)	0,99382	0,99680	-6,2	0,516	(Johnston et al., 2007; Johnston et al., 2005)
	Disproportion SO ₃ ²⁻ to H ₂ S Equation (9)	0,95500	0,97672	-45	0,511	(Johnston et al., 2005)*

*see next paragraph

Solid Sulfide Burial : Although Eldridge et al. (2021) have calculated fractionation factors for both ³³S and ³⁴S isotopes and for the different species of solid sulfide possibly generated through

aqueous sulfide reaction with iron, it is, in our case, difficult to assess the exact nature of the iron sulfide preserved in our samples that we extracted chemically. Moreover, it is most likely that we are in presence of different types of solid sulfide compounds possibly formed by different processes. Therefore, and given that the fractionation factors remain very small and are most likely to have a negligible effect on the isotopic signature of the iron sulfide in our samples (Eldridge et al., 2021; Fry et al., 1986), we consider that the fractionation during solid sulfide burial as negligible (see Table S3).

Abiotic oxidation : Because there are no known fractionation factors for abiotic sulfide oxidation by iron and manganese oxides, we considered, like (Pellerin et al., 2015) , that these processes fractionate sulfur isotopes similar to abiotic oxidation of sulfide by molecular oxygen (Eldridge et al., 2021).

4.2 Variable fractionation factor for microbial sulfate reduction

Multiple pure culture and environmental studies have found an inverse correlation between $csSRR$ and the magnitude of isotopic fractionation (see section 4.3.2 of the main text for further discussion on the use of $csSRR$ to model the range of variations expressed during MSR).

Leavitt et al. 2013, applied a nonlinear regression model (equations (12) and (13)) on the results of a pure culture experiment with microbial sulfate reducer *Desulfovibrio vulgaris hildenborough* (*DvH*) under constant sulfate concentration and variable concentration of the electron donor lactate:

$$csSRR = \frac{\ln\left(\frac{{}^{34}\epsilon_{Measured} - {}^{34}\epsilon_{Min}}{{}^{34}\epsilon_{Max} - {}^{34}\epsilon_{Min}}\right)}{-{}^{34}k_{msr}} \quad (12)$$

$$csSRR = \frac{\ln\left(\frac{{}^{33}\lambda_{Measured} - {}^{33}\lambda_{Min}}{{}^{33}\lambda_{Max} - {}^{33}\lambda_{Min}}\right)}{-{}^{33}k_{msr}} \quad (13)$$

where ${}^{34}\epsilon_{Measured}$ and ${}^{33}\lambda_{Measured}$ represent the extent of fractionation measured for each individual SO_4^{2-} - H_2S couple during the pure culture experiment, whereas ${}^{34}\epsilon_{Min}$, ${}^{33}\lambda_{Min}$, ${}^{34}\epsilon_{Max}$ and ${}^{33}\lambda_{Max}$ are the minimum and maximum empirical fractionations limits and ${}^{34}k_{msr}$ and ${}^{33}k_{msr}$ are pseudo first order rate constants obtained by fitting equations (12) and (13) to the experimental data.

Leavitt et al., 2013, however, explored only part of the potential fractionations possibly yielded by MSR communities because he only used lactate as an electron donor and set the sulfate concentration constant. On the other hand, Sim et al. (2011) carried out pure culture experiments with a variety of electron donors and sulfate concentrations, observing a wider range of isotope fractionations that approach the thermodynamic equilibrium between SO_4^{2-}

and H₂S equal to 70‰ (Brunner and Bernasconi, 2005; Farquhar et al., 2003; Tudge and Thode, 1950).

In our model, in order to cover the full range of isotopic fractionations that are possibly expressed by MSR activity, we expressed the cellular MSR rate of the Sim et al., 2011a, 2011b experiments on a normalized scale, where $csSRR=0$ corresponds to no sulfate reduction and $csSRR=100$ corresponds to the rate of sulfate reduction where the minimum isotope fractionation is expressed. We then refitted the data of Sim et al., 2011a, 2011b to equations (14) and (15) (Fig. S2). This allowed us to obtain our own $^{34}\epsilon_{Min}$ (-69), $^{33}\lambda_{Min}$ (0.511), $^{34}\epsilon_{Max}$ (-5), $^{33}\lambda_{Max}$ (0.515), $^{34}k_{msr}$ (0.0514) and $^{33}k_{msr}$ (0.1409) values.

In order to obtain the relationship that link $^{34}\epsilon$ and $^{33}\lambda$ to the normalized $csSRR$ we rearranged equation (13).

$$^{33}\lambda_{msr} = (e^{-csSRR \times ^{33}k_{msr}} (\lambda_{max} - \lambda_{min})) + \lambda_{min} \quad (14)$$

$$^{33}\alpha_{msr} = (^{34}\alpha_{msr}) ^{33}\lambda_{msr} \quad (15)$$

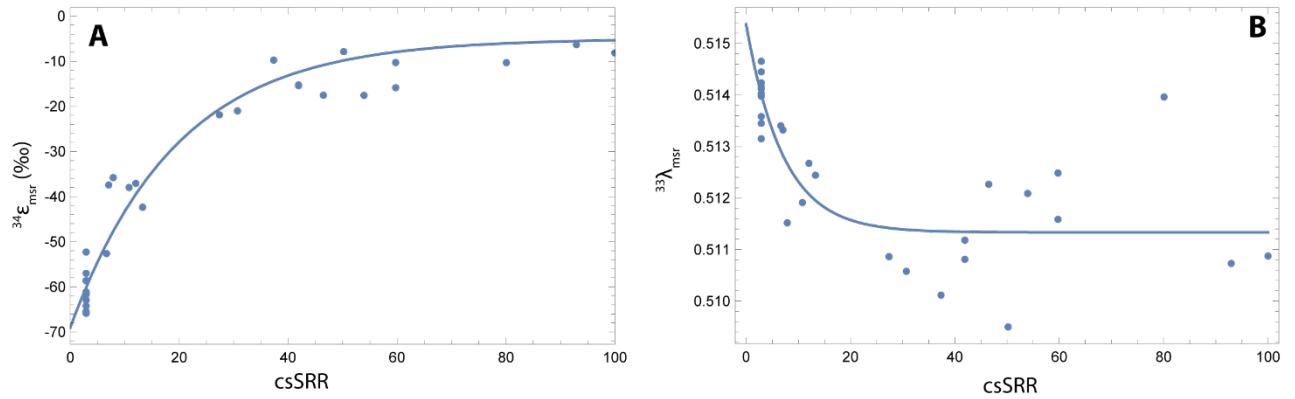


Figure S2: Nonlinear regression model fits using the equations from Leavitt et al., 2013 to major and minor sulfur isotope fractionations measured in experiments by Sim et al 2011 a and b. In both panels A et B paired sulfate-sulfide major $^{34}\epsilon_{msr}$ or minor $^{33}\lambda_{msr}$ observed fractionation factors are plotted against the recast $csSRR$ rate of MSR activity.

5. Model equations

As described in section 4.3.1 of the main text, the model is based on the chemical and isotopic mass balance for ^{34}S and ^{33}S sulfur isotope for SO_4^{2-} , S^0 and H_2S boxes (Main text Figure 6).

For the SO_4^{2-} box, the two mass balances are:

$$F_{in} + F_{do} + F_{riv} = F_{gyp} + F_{msr} + F_{out} \quad (16)$$

and

$$F_{in} \times R_{oc} + F_{do} \times R_{do} + F_{riv} \times R_{riv} = F_{gyp} \times R_{gyp} + F_{msr} \times R_{msr} + F_{out} \times R_{mb} \quad (17)$$

Where fluxes F_{in} and F_{out} are the exchange fluxes with the ocean, F_{riv} is the riverine flux, F_{gyp} is the gypsum precipitation flux, F_{msr} is the flux of sulfur reduced by MSR, F_{do} is the flux of sulfur being disproportionated sulfate.

R_x are the isotope ratios ($^{x}\text{S}/^{32}\text{S}$, where $x = 34$ or 33) of the same fluxes.

To obtain output fluxes of gypsum- and pyrite-S expressed as a percentage of the sulfur fluxes added to the marginal basin from external sources, we define:

$$F_{in} + F_{riv} = 100 \quad (18)$$

Furthermore, we define parameters (f_x , varying from 0 to 1) that express the relative magnitude of the different sulfur fluxes. Thus, f_{ex} represents the fraction of the incoming sulfur flux that is not involved in microbial reactions or gypsum precipitation:

$$f_{ex} = \frac{F_{out}}{(F_{in} + F_{riv})} \quad (19)$$

f_{riv} designates the fraction of the external sulfur inputs that is brought to the marginal basin by rivers:

$$f_{riv} = \frac{F_{riv}}{(F_{in} + F_{riv})} \quad (20)$$

and f_{msr} is the fraction of the net incoming sulfur flux being removed from the marginal basin through microbial sulfate reduction rather than by gypsum accumulation:

$$f_{msr} = \frac{F_{msr}}{(F_{in} + F_{riv} - F_{out})} \quad (21)$$

For the H₂S box, the two mass balances are:

$$F_{msr} + F_{dh} = F_{py} + F_{ox} \quad (22)$$

and

$$F_{msr} \times R_{msr} + F_{dh} \times R_{dh} = F_{py} \times R_{py} + F_{ox} \times R_{ox} \quad (23)$$

F_{py} is the flux of sulfur being buried as pyrite, F_{ox} is the flux of sulfur being reoxidised to sulfate or intermediate sulfur compound, F_{dh} is the flux of sulfur being disproportionated to sulfide. For the H_2S box, we define f_{ox} as the fraction of the incoming sulfur fluxes that leaves the H_2S box through H_2S -oxidation (reactions 3, 4, 5 or 6) instead of being precipitated as pyrite:

$$f_{ox} = \frac{F_{ox}}{(F_{msr} + F_{dh})} \quad (24)$$

For the S° box, the two mass balances are:

$$F_{ox} = F_{dh} + F_{do} \quad (25)$$

And

$$F_{ox} \times R_{ox} = F_{dh} \times R_{dh} + F_{do} \times R_{do} \quad (26)$$

For the S° box, we define f_{dh} as the fraction of sulfur added to the S° box by oxidation of H_2S that is re-reduced to H_2S through disproportionation:

$$f_{dh} = \frac{F_{dh}}{F_{ox}} \quad (27)$$

Fluxes associated to biogeochemical transformations or mineral formation have specific fractionation factors $^{34}\alpha$ and $^{33}\lambda$ defined in Table S3.

We define isotope fractionation factors for the considered processes that express a S-isotope fractionation:

$$\alpha_{gyp} = \frac{R_{gyp}}{R_{mb}} \quad (28)$$

is the fractionation factor associated to the precipitation of gypsum,

$$\alpha_{msr} = \frac{R_{msr}}{R_{mb}} \quad (29)$$

is the fractionation factor associated to microbial sulfate reduction

$$\alpha_{py} = \frac{R_{py}}{R_{H_2S}} \quad (30)$$

is the fractionation factor associated to pyrite formation

$$\alpha_{ox} = \frac{R_{ox}}{R_{H2S}} \quad (31)$$

is the fractionation factor associated to H2S oxidation

$$\alpha_{dh} = \frac{R_{dh}}{R_{S^\circ}} \quad (32)$$

is the fractionation factor associated to reduction of S° to H2S through S° disproportionation

$$\alpha_{do} = \frac{R_{do}}{R_{S^\circ}} \quad (33)$$

is the fractionation factor associated to oxidation of S° to SO4²⁻ through S° disproportionation

The set of 18 equations (22 to 33) and 18 unknowns ($F_{in}, F_{ox}, F_{riv}, F_{out}, F_{gyp}, F_{py}, F_{msr}, F_{dh}, F_{do}, R_{SO4}, R_{gyp}, R_{py}, R_{H2S}, R_{ox}, R_{msr}, R_{do}, R_{dh}, R_{S^\circ}$) was solved analytically with the Wolfram Mathematica 11 software, providing mathematical expressions for all sulfur fluxes and their isotope ratios (equations 37 to 54, below).

To facilitate reading of equations (39) to (56), we define:

$$A = \alpha_{gyp}(f_{ex} - 1)(1 + f_{msr}(f_{ox} - 1) - f_{dh}f_{ox}) \quad (34)$$

$$B = -f_{ex} + \alpha_{msr}f_{msr}(f_{ex} - 1)(f_{dh}f_{ox} - 1) \quad (35)$$

$$C = \alpha_{py}(f_{ox} - 1) \quad (36)$$

$$D = (f_{dh}f_{ox} - 1)(R_{oc}(f_{riv} - 1) - \alpha_{riv}R_{riv})$$

Following these new notations, solutions of equations (22) to (35) are given below

$$F_{in} = -100(f_{riv} - 1) \quad (37)$$

$$F_{riv} = 100f_{riv} \quad (38)$$

$$F_{out} = 100 \times f_{ex} \quad (39)$$

$$F_{msr} = -100f_{msr}(f_{ex} - 1) \quad (40)$$

$$F_{ox} = -\frac{F_{msr}f_{ox}}{f_{dh}f_{ox}-1} \quad (41)$$

$$F_{dh} = F_{ox}f_{dh} \quad (42)$$

$$F_{do} = -F_{ox}(f_{dh} - 1) \quad (43)$$

$$F_{gyp} = -\frac{F_{ox}(f_{msr}+f_{dh}f_{ox}-f_{msr}f_{ox}-1)}{f_{msr}f_{ox}} \quad (44)$$

$$F_{py} = \frac{F_{msr}(f_{ox}-1)}{(f_{dh}f_{ox}-1)} \quad (45)$$

$$R_{SO4} = \frac{D[-\alpha_{dh}f_{dh}C + \alpha_{do}(f_{dh}-1)(C - \alpha_{ox}f_{ox})]}{[\alpha_{dh}f_{dh}C(A-B)] + \alpha_{do}(f_{dh}-1)[(BC + \alpha_{ox}f_{ox}f_{ex}(f_{dh}f_{ox}-1) - A(C - \alpha_{ox}f_{ox}))]} \quad (46)$$

$$R_{msr} = R_{SO4} \alpha_{msr} \quad (47)$$

$$R_{gyp} = R_{SO4} \alpha_{gyp} \quad (48)$$

$$R_{H2S} = \frac{D \alpha_{msr} (f_{dh} f_{ox} - 1) [\alpha_{do} (f_{dh} - 1) - \alpha_{dh} f_{dh}]}{[\alpha_{dh} f_{dh} C(A-B)] + \alpha_{do} (f_{dh} - 1) [(BC + \alpha_{ox} f_{ox} f_{ex} (f_{dh} f_{ox} - 1) - A(C - \alpha_{ox} f_{ox}))]} \quad (49)$$

$$R_{py} = R_{H2S} \alpha_{py} \quad (50)$$

$$R_{ox} = R_{H2S} \alpha_{ox} \quad (51)$$

$$R_{do} = -R_{H2S} \alpha_{ox} \alpha_{do} \quad (52)$$

$$R_{dh} = -R_{H2S} \alpha_{ox} \alpha_{dh} \quad (53)$$

$$R_{S^{\circ}} = -\frac{R_{H2S} \alpha_{ox}}{[\alpha_{do} (f_{dh} - 1) - \alpha_{dh} f_{dh}]} \quad (54)$$

To this set of equations were added equations (12), (14) and (15) that allowed to explore the full range of MSR fractionation.

6. Fixed Parameters

The isotopic composition of riverine input was set equal to the average values of modern rivers ($\delta^{34}S_{SO4}=4.8\text{‰}$ (Burke et al., 2018) and $\Delta^{33}S_{SO4}=-0.0187\text{‰}$ (Tostevin et al., 2014)). Based on the observation by Topper et al. (2011) that riverine inputs contributed for 10 to 80% of the total water inputs during PLG formation and on the fact that freshwater inputs are approximately 100 times less concentrated than oceanic waters in sulfate ion (Burke et al., 2018), we calculated that the fraction of incoming sulfate originating from riverine inputs on the total sulfate input, f_{riv} , ranged between 0 and 0.075, we fixed it here at 0.035. This is consistent with the blue mixing curve displayed on figure 4 that describe the mixing between oceanic sulfate and riverine inputs and from which can be inferred that the riverine inputs had a negligible influence on the sulfate isotopic composition of gypsum.

We then fixed the external basin sulfate isotopic composition equal to that of the sulfate from the first gypsum bed of the Vena del Gesso basin ($\delta^{34}\text{S}_{\text{SO}_4}=21.78\text{‰}$ and $\Delta^{33}\text{S}_{\text{SO}_4}=0.033\text{‰}$). This isotope composition is very close to that of sulfate dissolved in the global Messinian ocean ($\delta^{34}\text{S}_{\text{MESS}}=22.16\pm 0.3 \text{‰}$ and $\Delta^{33}\text{S}_{\text{MESS}}= 0.035 \pm 0.013 \text{‰}$ (Masterson et al., 2016)). Hydrochemical models of the MSC suggest that during deposition of PLG a two-way (inflow-outflow) water exchange always existed between the Mediterranean Sea and the Atlantic Ocean, and between the marginal basins and the main Mediterranean basin (Topper et al., 2014). At the acme of gypsum precipitation in a marginal basin connected to the Mediterranean sea, Topper and Meijer (2015) calculated that calcium sulfate concentration in the marginal basin is approximately 1.2 times greater than in the main Mediterranean basin, whereas the water outflow represents 69 to 77% of the water inflow from the main Mediterranean basin. This allowed us to estimate that the fraction of sulfate output from the Vena del Gesso basin to the Mediterranean represented between 87 and 96% of the incoming sulfate fluxes; thus, we set f_{ex} equal to 0.9 to represent sulfate exchanges with the external sulfate source during gypsum precipitation.

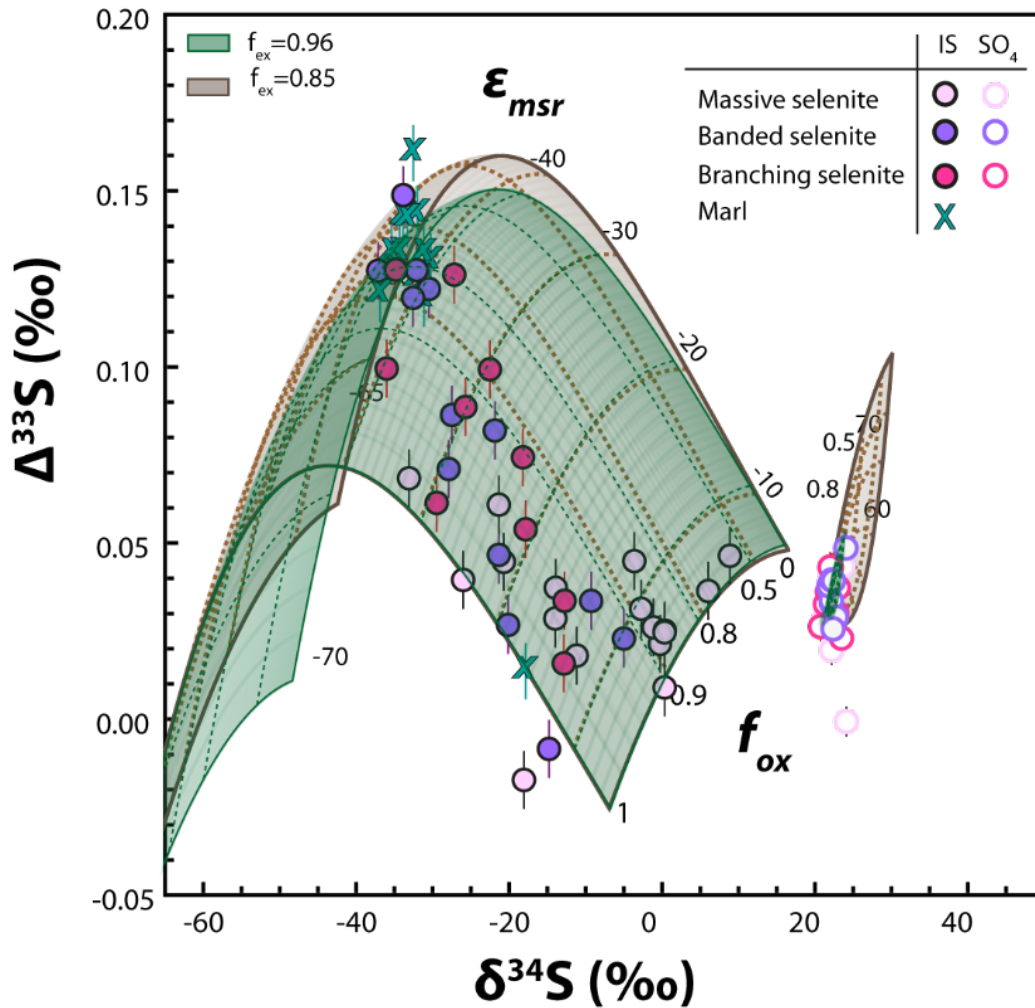


Figure S3: Sensitivity test for varying values of f_{ex} of 0.96 (green area) and 0.85 (brown area). The main differences from our best fit results (where $f_{ex} = 0.9$) concern the sulfate isotopic values, with the area covered being smaller when the chosen f_{ex} is larger, possibly requiring a larger f_{msr} to explain the whole range of values covered by our sulfate data (see supplementary section 6 for further explanation on this point).

The amount of intermediate sulfur compound being disproportionated into sulfide f_{dh} is the complement of f_{do} , the amount of intermediate sulfur compound being disproportionated into sulfate. f_{dh} was chosen depending on the scenario tested, with $f_{dh} = 0$ when the model was tested for the absence of reoxidation or disproportionation, $f_{dh} = 0.25$ when we tested the model for disproportionation of sulfite and $f_{dh} = 0.75$ when the elemental sulfur disproportionation scenario was chosen (see Pellerin et al., 2015 and references therein for stoichiometry of

disproportionation reactions). Finally, the entire range of values for the fraction of sulfur reduced through MSR ($0 < f_{msr} < 1$) was tested in order to find the f_{msr} that would best fit our data (see supplementary information).

7. Constrains on f_{msr}

In the $^{34}\epsilon\text{-}^{33}\lambda$ space, model results depend only on the magnitude of the isotope fractionation associated to MSR and on the fluxes (f_{ox} and f_{dh}) and fractionation factors (α_{ox} , α_{dh} and α_{do}) controlling the reoxidative part of the sulfur cycle. Therefore, the $^{34}\epsilon_{net}\text{-}^{33}\lambda_{net}$ dataset (built considering samples that have a paired sulfate-iron sulfide isotope composition), is used to constrain f_{ox} and ϵ_{MSR} . Most of the $^{34}\epsilon_{net}\text{-}^{33}\lambda_{net}$ data is reproduced by the model only if $f_{ox} > 0.85$ and $\epsilon_{MSR} > -50\%$ (Main text Fig.8b).

Instead, in the $\delta^{34}\text{S}\text{-}\Delta^{33}\text{S}$ space, the model results are a function of all sulfur fluxes and fractionation factors, and thus also of f_{msr} (Fig. 8a). Thus, with f_{ox} and ϵ_{MSR} constrained as explained above, f_{msr} can be constrained considering the $\delta^{34}\text{S}\text{-}\Delta^{33}\text{S}$ dataset (Fig. S3). The sulfate isotope composition of VdG samples spans a small range from 20.7 to 24.1 ‰ in $\delta^{34}\text{S}$ and from -0.001 to 0.0049 in $\Delta^{33}\text{S}$. In the $\delta^{34}\text{S}\text{-}\Delta^{33}\text{S}$ space, the size of the area corresponding to the full considered range of f_{ox} and ϵ_{MSR} depends on f_{msr} : small values of f_{msr} produce a limited isotope reservoir effect, and thus a small deviation of model results from the initial basin sulfate composition, while elevated f_{msr} values result in a strong isotope reservoir effect and a large area defined by the model results (Fig. S3). With the constraints on f_{ox} and ϵ_{MSR} introduced above ($f_{ox} > 0.85$, $\epsilon_{MSR} > -50\%$), only values of $f_{msr} > 0.8$ result in a good fit of the model to the sulfate data in the $\delta^{34}\text{S}_{\text{SO}_4}\text{-}\Delta^{33}\text{S}_{\text{SO}_4}$ space (Fig. S3).

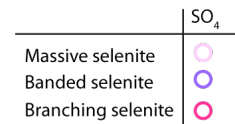
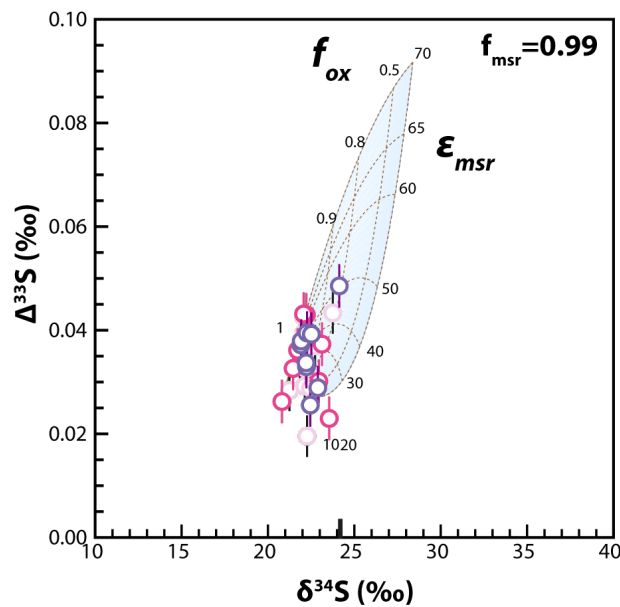
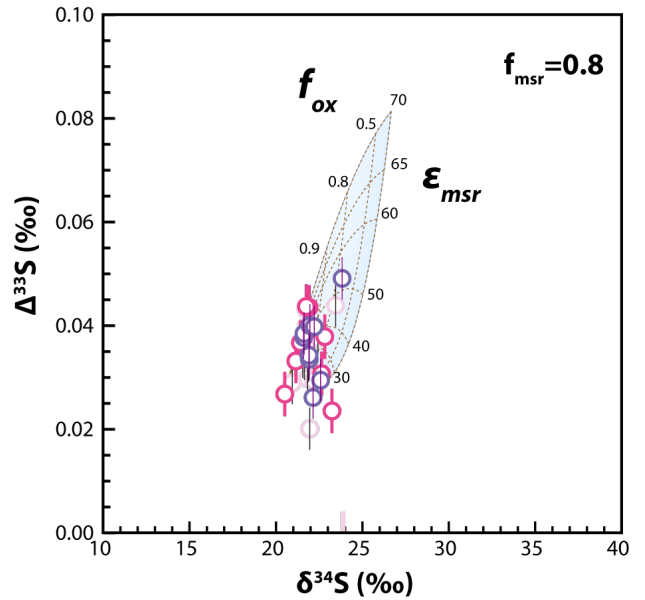
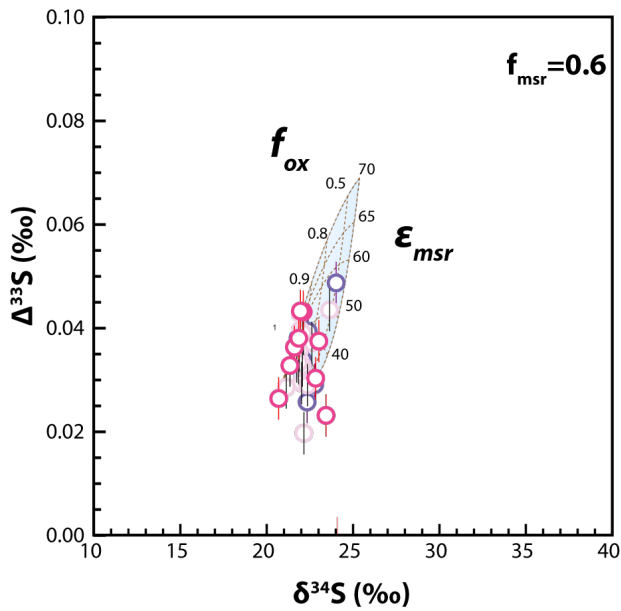
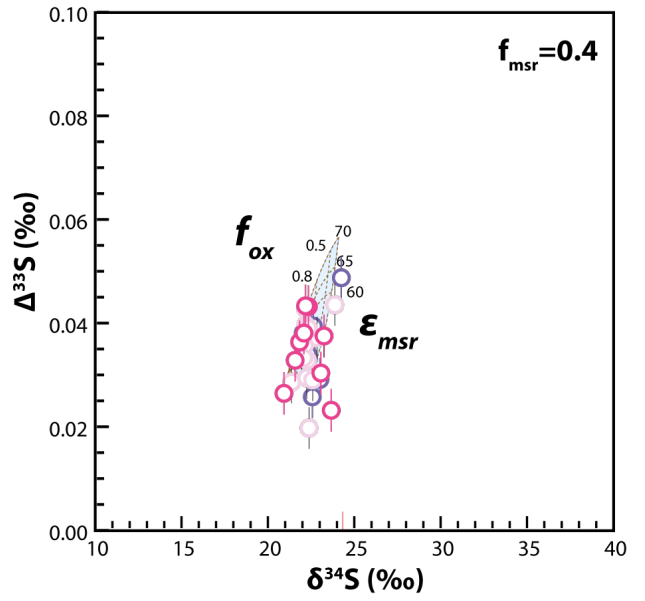
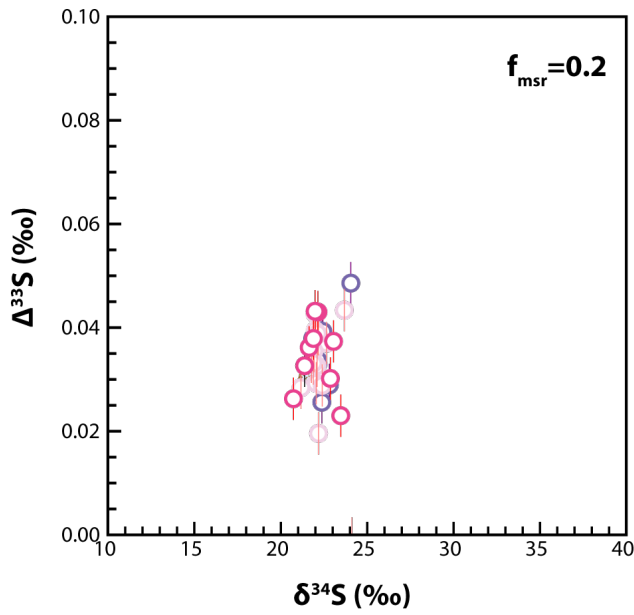


Figure S4: Figure 7: Measured and modelled $\Delta^{33}\text{S}_{\text{SO}_4}$ vs $\delta^{34}\text{S}_{\text{SO}_4}$ best fit with different values of f_{msr} . Individual curves represent the modelled isotopic composition sulfate data from gypsum samples for $0 < f_{\text{ox}} < 1$ and $0 < \text{csSRR} < 100$.

8. Supplementary discussion on the reoxidative portion of the sulfur cycle

In the best fit model run (Main text Fig. 8), the use of fractionation factors and sulfur fluxes typical of elemental sulfur redox processing is in good agreement with the occurrence of iron sulfides associated with the remains of CSB in our samples, interpreted to result from early diagenesis of elemental sulfur. However, the nature of the microbial process driving the reoxidative portion of this cryptic sulfur cycle is still uncertain. The best fit model run is based on the combination of sulfide oxidation to S^0 by chemolithotrophs biofilms and subsequent microbial S^0 disproportionation (main text Fig. 8), because multiple sulfur isotope fractionation for these processes have been determined (Supplementary Table S3). However, the available isotope data for pure culture of sulfide-oxidizer is scant and we cannot exclude that other re-oxidative processes involving the S^0 intermediate produce a comparable isotope fractionation. In particular, the abundance of microbial fossils indicating the presence of CSB mats in Vena del Gesso gypsum makes these microorganisms the best possible alternative. To our knowledge, there are no experimental studies of sulfur fractionation by pure cultures of CSB. However, CSB being chemolithotrophs, and the biofilms from which comes the fractionation factors we used for our best fit for the oxidation of H_2S to S^0 being dominated by chemolithotrophs organisms, it is likely that CSB produce a similar isotopic fractionation than the one we used while oxidizing H_2S . Note that the occurrence of a reoxidative sulfur cycling involving the fractionation factors for elemental sulfur disproportionation has been previously suggested in porewaters displaying similar higher $^{33}\lambda_{\text{net}}$ than maximal λ_{MSR} and in the presence

of Beggiatoa CSB (Pellerin et al., 2015). Thus, our data and modelling imply that the cryptic sulfur cycle was driven by MSR and a re-oxidative process isotopically consistent with H₂S oxidation to S⁰ and subsequent elemental S⁰ disproportionation, possibly involving the metabolism of CSB.

9. Other biogeochemical scenarios

In order to find a best fit to our data, we tested several scenarios involving different pathways for sulfur redox cycling. In all the tested scenarios the full range of f_{ox} (the relative amount of sulfide being oxidated into sulfate or intermediate sulfur compound) and ϵ_{MSR} (the extent of isotopic fractionation during MSR) were explored.

The amount of intermediate sulfur compound being disproportionated into sulfide f_{dh} is the complement of f_{do} , the amount of intermediate sulfur compound being disproportionated into sulfate. f_{dh} was chosen depending on the scenario tested, as explained below.

The occurrence of MSR without subsequent reoxidation was tested with attributing a $f_{ox}=0$, $f_{dh}=0$ and varying f_{msr} and ϵ_{MSR} (Fig. S5). In $\Delta^{33}\text{S}-\delta^{34}\text{S}$ diagram whereas our iron sulfide data does not fit the model, SO₄ data could be explained by low values of ϵ_{MSR} and f_{msr} . In the $^{34}\epsilon_{net}$ and $^{33}\lambda_{net}$ diagram, the model produces a curve that does not fit our data. Note that in the absence of reoxidation the model in the $^{34}\epsilon_{net}$ and $^{33}\lambda_{net}$ is not an area but a curve following the different values of csSRR. This shows that the value of f_{msr} used in the $^{34}\epsilon$ - $^{33}\lambda$ space has no influence on the isotopic fractionation expressed.

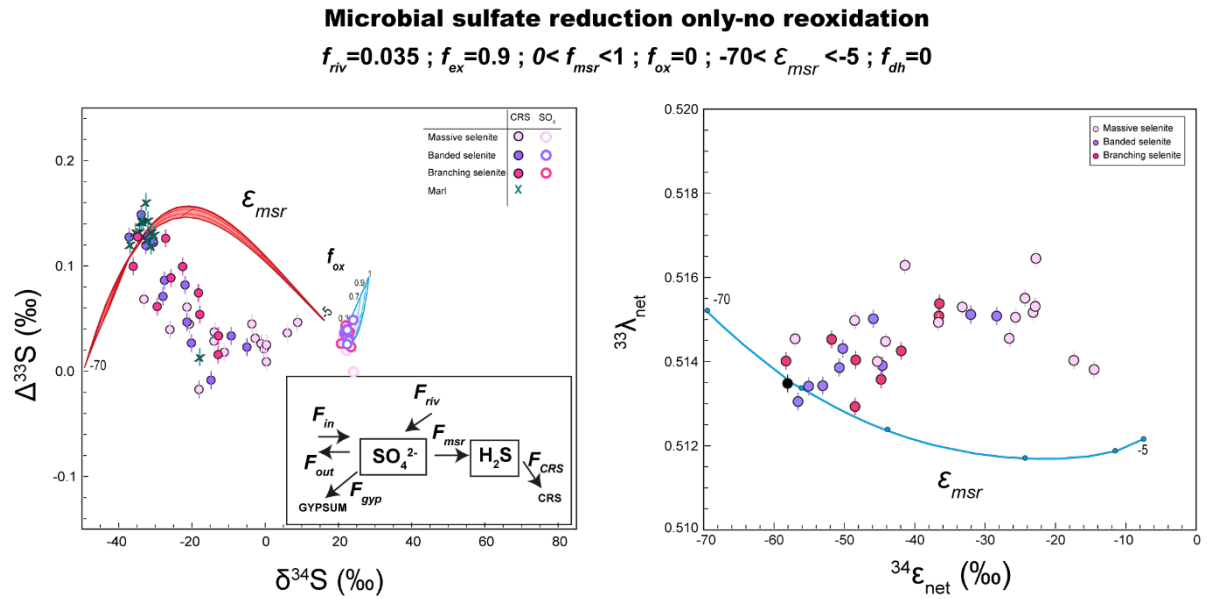


Figure S5: Measured and modelled $\Delta^{33}S_{SO_4}$ and $\Delta^{33}S_{IS}$ vs $\delta^{34}S_{SO_4}$ and $\delta^{34}S_{IS}$ data in **A** and $^{34}\epsilon_{net}$ and $^{33}\lambda_{net}$ in **B** with the model fluxes and fractionation factors chosen for a scenario where there is no reoxidation of H_2S . Individual curves represent the modelled isotopic composition in **A** and net fractionations factor for paired sulfate-sulfide data from the same gypsum samples in **B** for different values of f_{msr} and ϵ_{MSR} . f_{msr} is the fraction of the net incoming sulfur flux being removed from the marginal basin through microbial sulfate reduction rather than by gypsum accumulation and $csSRR$ the extent of ^{34}S isotopic fractionation during MSR. Mathematical relationship between the fluxes of sulfur F_x and the relative magnitude of these fluxes f_x are given in section 5.

For each of the subsequent scenarios different values of f_{msr} (from 0 to 1) were tested in order to find a best fit to our data. This allowed us to understand what fraction of sulfate from the basin has been reduced through microbial sulfate reduction activity during PLG formation.

The direct reoxidation of hydrogen sulfide to sulfate was tested by combining the fractionation factors α_{ox} for the reoxidative flux f_{ox} attributed to equations 3, 4 or 5 (inorganic oxidation) or 6 (phototrophic oxidation) to $f_{dh}=0$ (implying $f_{do}=1$) and no fractionation for the disproportionation flux α_{dh} (Fig. S6). In both $\Delta^{33}S$ - $\delta^{34}S$ and $^{34}\epsilon$ and $^{33}\lambda$ the model does not cover the full range of values expressed in our samples, supporting our conclusions that the

filamentous fossils found in gypsum does not corresponds to cyanobacteria remains (Panieri et al., 2008) but to CSB remains (Dela Pierre et al., 2015; Natalicchio et al., 2022; Schopf et al., 2012). Note that in the model that consider phototrophic oxidation of hydrogen sulfide, low ϵ_{MSR} and f_{ox} values in the model approach the values obtained for iron sulfide in marls, which is in good agreement with periodic euxinia during marl deposition (Fig. S5). This support the observation by Sinninghe Damsté et al. (1995) that have found abundant lipid biomarkers indicative of phototrophic green sulfur bacteria within the marls.

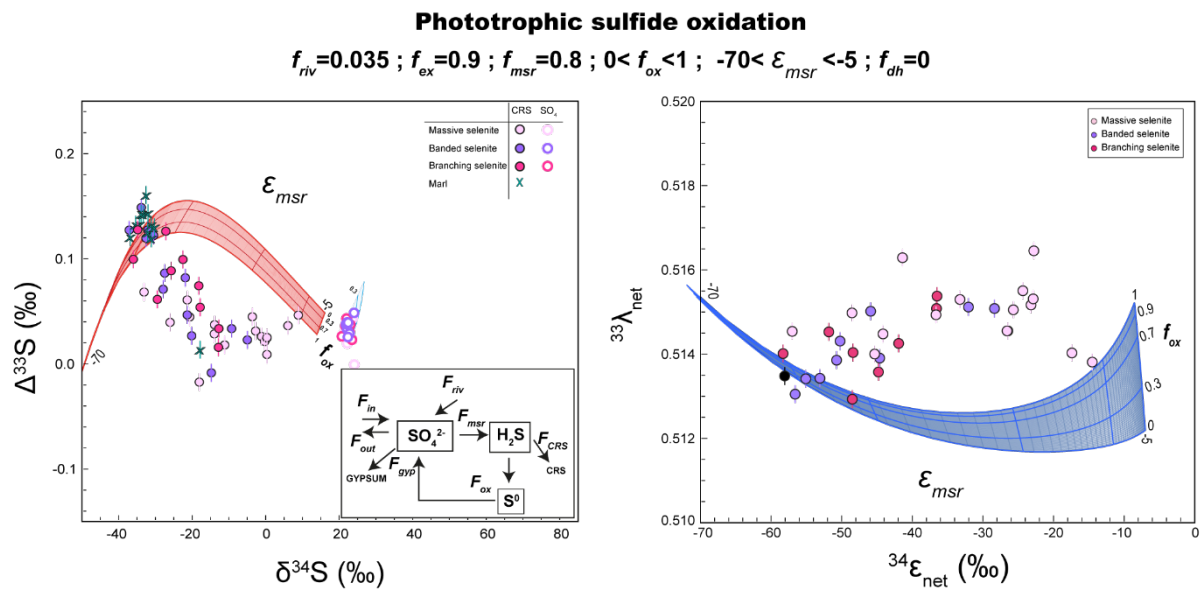


Figure S6: Measured and modelled $\Delta^{33}S_{SO_4}$ and $\Delta^{33}S_{IS}$ vs $\delta^{34}S_{SO_4}$ and $\delta^{34}S_{IS}$ data in **A** and $^{34}\epsilon_{net}$ and $^{33}\lambda_{net}$ in **B** with the model fluxes and fractionation factors chosen for the phototrophic reoxidation scenario. Individual curves represent the modelled isotopic composition in **A** and net fractionations factor for paired sulfate-sulfide data from the same gypsum samples in **B** for different values of f_{msr} and $csSRR$. f_{msr} is the fraction of the net incoming sulfur flux being removed from the marginal basin through microbial sulfate reduction rather than by gypsum accumulation and $csSRR$ the cellular rate of microbial sulfate reduction. Mathematical relationship between the fluxes of sulfur F_x and the relative magnitude of these fluxes f_x are given in section 5.

We weren't able to test the hypothesis of a complete oxidation of sulfide into sulfate by chemolithotrophic bacteria because no fractionation factors are so far available in the literature (see section 4.1 above).

The disproportionation of elemental sulfur into sulfide was tested by combining the fractionation factors α_{ox} for the reoxidative flux attributed to equations 6.1 (phototrophic oxidation) or 7.1 (chemolithotrophic oxidation) to $f_{dh}=0.75$ (implying $f_{do}=0.25$) (see the best fit Fig.8 in the main text) in agreement with the stoichiometry of the reaction (Thamdrup et al., 1993) whereas the disproportionation of sulfite was tested by using $f_{dh}=0.25$ ($f_{do}=0.75$) (Bak and Cypionka, 1987) (Fig. S7). As the fractionation factors of paired ^{33}S and ^{34}S isotopes for the oxidation of aqueous sulfide into sulfite remains unknown, when we tested our model for disproportionation of sulfite, the production of sulfite was done by testing all the fractionation factors available for aqueous sulfide oxidation (equations 3,4,5,6.1 and 7.1).

Whereas the areas covered by our model are larger than for previous scenarios (Fig. S7), allowing to fit a larger set of data point with the model, this scenario still doesn't reproduce the whole range of isotopic data we measured for the Vena del Gesso section. Moreover, the occurrence of remains of sulfur globules in our samples point its greater implication compared to sulfite as an intermediate sulfur compound in the genesis of the observed isotopic signatures of our samples.

Abitotic oxidation of H_2S to SO_3^{2-} + disproportionation of SO_3^{2-}

$$f_{riv}=0.035; f_{ex}=0.9; f_{msr}=0.8; 0 < f_{ox} < 1; -70 < \epsilon_{msr} < -5; f_{dh}=0.25$$

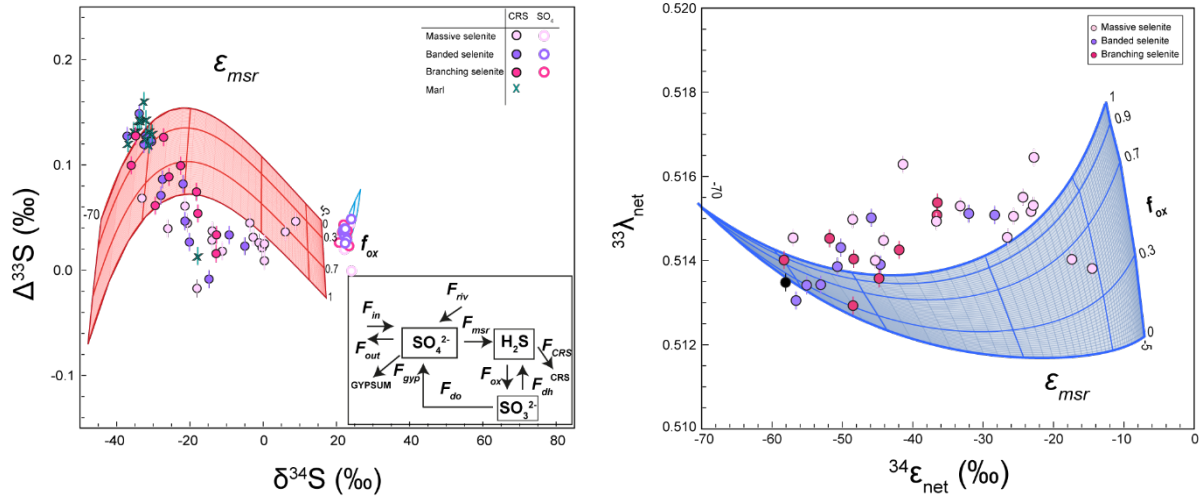


Figure S7: Measured and modelled $\Delta^{33}\text{S}_{\text{SO}_4}$ and $\Delta^{33}\text{S}_{\text{IS}}$ vs $\delta^{34}\text{S}_{\text{SO}_4}$ and $\delta^{34}\text{S}_{\text{IS}}$ data in **A** and $^{33}\lambda_{\text{net}}$ in **B** with the model fluxes and fractionation factors chosen for the abiotic oxidation of H_2S into SO_3^{2-} and its subsequent disproportionation. Individual curves represent the modelled isotopic composition in **A** and net fractionations factor for paired sulfate-sulfide data from the same gypsum samples in **B** for different values of f_{msr} and $cs\text{SRR}$. f_{msr} is the fraction of the net incoming sulfur flux being removed from the marginal basin through MSR rather than by gypsum accumulation and $cs\text{SRR}$ the cellular rate of microbial sulfate reduction. Mathematical relationship between the fluxes of sulfur F_x and the relative magnitude of these fluxes f_x are given in section 5.

Bibliography

- Aller, R.C. and Rude, P.D. (1988) Complete oxidation of solid phase sulfides by manganese and bacteria in anoxic marine sediments. *Geochimica et Cosmochimica Acta* 52, 751-765.
- Aref, M. (2003) Lithofacies characteristics, depositional environment and karstification of the Late Miocene (Messinian) gypsum deposits in the Northern Western Desert, Egypt. *Sedimentology of Egypt* 11, 9-27.
- Avrahami, M. and Golding, R.M. (1968) The oxidation of the sulphide ion at very low concentrations in aqueous solutions. *Journal of the Chemical Society A: Inorganic, Physical, Theoretical*, 647-651.
- Bak, F. and Cypionka, H. (1987) A novel type of energy metabolism involving fermentation of inorganic sulphur compounds. *Nature* 326, 891-892.
- Balci, N., Shanks III, W.C., Mayer, B. and Mandernack, K.W. (2007) Oxygen and sulfur isotope systematics of sulfate produced by bacterial and abiotic oxidation of pyrite. *Geochimica et Cosmochimica Acta* 71, 3796-3811.
- Bertran, E., Leavitt, W.D., Pellerin, A., Zane, G.M., Wall, J.D., Halevy, I., Wing, B.A. and Johnston, D.T. (2018) Deconstructing the Dissimilatory Sulfate Reduction Pathway: Isotope Fractionation of a Mutant Unable of Growth on Sulfate. *Frontiers in Microbiology* 9.
- Boschetti, T., Cortecchi, G., Toscani, L. and Iacumin, P. (2011) Sulfur and oxygen isotope compositions of Upper Triassic sulfates from Northern Apennines (Italy): palaeogeographic and hydrogeochemical implications. *Geologica Acta*, 129-147.
- Boulton, S.J., Smart, C.W., Consolaro, C. and Snider, A. (2016) The Miocene–Pliocene boundary and the Messinian Salinity Crisis in the easternmost Mediterranean: Insights from the Hatay Graben (Southern Turkey). *Sedimentary Geology* 332, 51-67.
- Brand, W.A., Coplen, T., B. , Vogl, J., Rosner, M. and Prohaska, T. (2014) Assessment of international reference materials for isotope-ratio analysis (IUPAC Technical Report). *Pure and Applied Chemistry* 86, 425-467.
- Brunner, B. and Bernasconi, S. (2005) A revised isotope fractionation model for dissimilatory sulfate reduction in sulfate reducing bacteria. *Geochimica et Cosmochimica Acta* 69, 4759-4771.
- Burke, A., Present, T.M., Paris, G., Rae, E.C.M., Sandilands, B.H., Gaillardet, J., Peucker-Ehrenbrink, B., Fischer, W.W., McClelland, J.W., Spencer, R.G.M., Voss, B.M. and Adkins, J.F. (2018) Sulfur isotopes in rivers: Insights into global weathering budgets, pyrite oxidation, and the modern sulfur cycle. *Earth and Planetary Science Letters* 496, 168-177.
- Claypool, G.E., Holser, W.T., Kaplan, I.R., Sakai, H. and Zak, I. (1980) The age curves of sulfur and oxygen isotopes in marine sulfate and their mutual interpretation. *Chemical Geology* 28, 199-260.
- Cohen, A. (1993) Halite-clay interplay in the Israeli Messinian. *Sedimentary Geology* 86, 211-228.
- Costanzo, A., Cipriani, M., Feely, M., Cianflone, G. and Dominici, R. (2019) Messinian twinned selenite from the Catanzaro Trough, Calabria, Southern Italy: field, petrographic and fluid inclusion perspectives. *Carbonates and Evaporites* 34, 743-756.
- Crockford, P.W., Kunzmann, M., Bekker, A., Hayles, J., Bao, H., Halverson, G.P., Peng, Y., Bui, T.H., Cox, G.M., Gibson, T.M., Wörndle, S., Rainbird, R., Lepland, A., Swanson-Hysell, N.L., Master, S., Sreenivas, B., Kuznetsov, A., Krupenik, V. and Wing, B.A. (2019) Claypool continued: Extending the isotopic record of sedimentary sulfate. *Chemical Geology* 513, 200-225.

Damsté, S.J.S., Frewin, N.L., Kenig, F. and De Leeuw, J.W. (1995) Molecular indicators for palaeoenvironmental change in a Messinian evaporitic sequence (Vena del Gesso, Italy). I: Variations in extractable organic matter of ten cyclically deposited marl beds. *Organic Geochemistry* 23, 471-483.

Dela Pierre, F., Natalicchio, M., Ferrando, S., Giustetto, R., Birgel, D., Carnevale, G., Gier, S., Lozar, F., Marabello, D. and Peckmann, J. (2015) Are the large filamentous microfossils preserved in Messinian gypsum colorless sulfide-oxidizing bacteria? *Geology* 43, 855-858.

El Euch-El Koundi, N., Ferry, S., Suc, J.-P., Clauzon, G., Melinte-Dobrinescu, M., Gorini, C., Safra, A. and Zargouni, F. (2009) Messinian deposits and erosion in northern Tunisia: Inferences on Strait of Sicily during the Messinian Salinity Crisis. *Terra Nova* 21, 41-48.

El Kilany, A. (2018) Hydrologie et cycles biogéochimiques du soufre dans deux bassins marginaux de Méditerranée pendant la Crise de Salinité Messinienne, LOCEAN - Laboratoire d'Océanographie et du Climat : Expérimentations et Approches Numériques Université Sorbonne Paris Cité p. 274.

Eldridge, D., Kamyshny, A. and Farquhar, J. (2021) Theoretical estimates of equilibrium sulfur isotope effects among aqueous polysulfur and associated compounds with applications to authigenic pyrite formation and hydrothermal disproportionation reactions. *Geochimica et Cosmochimica Acta*.

Eldridge, D.L. and Farquhar, J. (2018) Rates and multiple sulfur isotope fractionations associated with the oxidation of sulfide by oxygen in aqueous solution. *Geochimica et Cosmochimica Acta* 237, 240-260.

Evans, N.P., Turchyn, A.V., Gázquez, F., Bontognali, T.R., Chapman, H.J. and Hodell, D.A. (2015) Coupled measurements of $\delta^{18}\text{O}$ and δD of hydration water and salinity of fluid inclusions in gypsum from the Messinian Yesares Member, Sorbas Basin (SE Spain). *Earth and Planetary Science Letters* 430, 499-510.

Farquhar, J., Johnston, D.T., Wing, B.A., Habicht, K.S., Canfield, D.E., Airieau, S. and Thiemens, M.H. (2003) Multiple sulphur isotopic interpretations of biosynthetic pathways: implications for biological signatures in the sulphur isotope record. *Geobiology* 1, 27-36.

Findlay, A.J., Di Toro, D.M. and Luther lii, G.W. (2017) A model of phototrophic sulfide oxidation in a stratified estuary. *Limnology and Oceanography* 62, 1853-1867.

Fry, B., Cox, J., Gest, H. and Hayes, J.M. (1986) Discrimination between ^{34}S and ^{32}S during bacterial metabolism of inorganic sulfur compounds. *J Bacteriol* 165, 328-330.

García-Veigas, J., Cendón, D.I., Gibert, L., Lowenstein, T.K. and Artiaga, D. (2018) Geochemical indicators in Western Mediterranean Messinian evaporites: Implications for the salinity crisis. *Marine Geology* 403, 197-214.

Geng, L., Savarino, J., Savarino, C.A., Caillon, N., Cartigny, P., Hattori, S., Ishino, S. and Yoshida, N. (2018) A simple and reliable method reducing sulfate to sulfide for multiple sulfur isotope analysis. *Rapid Commun Mass Spectrom* 32, 333-341.

Hardenberg, M.F. and Robertson, A.H.F. (2007) Sedimentology of the NW margin of the Arabian plate and the SW-NE trending Nahr El-Kabir half-graben in northern Syria during the latest Cretaceous and Cenozoic. *Sedimentary Geology* 201, 231-266.

Harrab, S., Mannai-Tayech, B., Rabhi, M. and Zargouni, F. (2013) Study of a Neogene basin dynamics: The "Bizerte basin", northeastern Tunisia: relevance to the global Messinian Salinity Crisis. *Comptes Rendus Geoscience* 345, 251-261.

Hsü, K., Montadert, L., Bernoulli, D., Bizon, G., Cita, M., Erickson, A., Fabricius, F., Garrison, R., Kidd, R. and Melieres, F. (1978a) Site 371: South Balearic Basin. Initial Reports of the Deep Sea Drilling Project 42, 29-57.

Hsü, K., Montadert, L., Bernoulli, D., Bizon, G., Cita, M., Erickson, A., Fabricius, F., Garrison, R., Kidd, R. and Mélières, F. (1978b) Site 378: Cretan Basin. Initial Rep. Deep Sea Drill. Proj 42, 321-357.

Hsü, K., Montadert, L., Bernoulli, D., Bizon, G., Cita, M., Erickson, A., Fabricius, F., Garrison, R., Kidd, R. and Mélières, F. (1978c) Sites 375 and 376: Florence Rise. Initial Reports of the Deep-Sea Drilling Project. Edited by KJ Hsü and L. Montadert 42, 219-304.

Hsü, K., Montadert, L., Bernoulli, D., Bizon, G., Cita, M., Erickson, A. and Wright, R. (1978d) Site 374: Messina abyssal plain. Initial Rep. Deep Sea Drill. Proj 42, 175-217.

Hsü, K.J., Ryan, W.B.F. and Cita, M.B. (1973) Late Miocene Desiccation of the Mediterranean. *Nature* 242, 240-244.

Johnston, D.T., Farquhar, J. and Canfield, D.E. (2007) Sulfur isotope insights into microbial sulfate reduction: When microbes meet models. *Geochimica et Cosmochimica Acta* 71, 3929-3947.

Johnston, D.T., Farquhar, J., Wing, B.A., Kaufman, A.J., Canfield, D.E. and Habicht, K.S. (2005) Multiple sulfur isotope fractionations in biological systems: A case study with sulfate reducers and sulfur disproportionators. *American Journal of Science* 305, 645-660.

Johnston, D.T., Gill, B.C., Masterson, A., Beirne, E., Casciotti, K.L., Knapp, A.N. and Berelson, W. (2014) Placing an upper limit on cryptic marine sulphur cycling. *Nature* 513, 530-533.

Jovovic, I., Grossi, V., Adam, P., Simon, L., Antheaume, I., Gelin, F., Ader, M. and Cartigny, P. (2020) Quantitative and specific recovery of natural organic and mineral sulfur for (multi-)isotope analysis. *Organic Geochemistry* 146, 104055.

Karakitsios, V., Roveri, M., Lugli, S., Manzi, V., Gennari, R., Antonarakou, A., Triantaphyllou, M., Agiadi, K., Kontakiotis, G., Kafousia, N. and de Rafelis, M. (2017) A record of the Messinian salinity crisis in the eastern Ionian tectonically active domain (Greece, eastern Mediterranean). *Basin Research* 29, 203-233.

Kastens, K., Mascle, J. and Auroux, C. (1987) Site 654: Upper sardinian margin. Kastens, KA, et al., *Proceedings of the Ocean Drilling Program, Initial reports* 107, 747-875.

Krijgsman, W., Hilgen, F.J., Raffi, I., Sierro, F.J. and Wilson, D.S. (1999) Chronology, causes and progression of the Messinian salinity crisis. *Nature* 400, 652-655.

Leavitt, W.D., Halevy, I., Bradley, A.S. and Johnston, D.T. (2013) Influence of sulfate reduction rates on the Phanerozoic sulfur isotope record. *Proceedings of the National Academy of Sciences* 110, 11244.

Lloyd, R.M. (1968) Oxygen isotope behavior in the Sulfate-Water System. *Journal of Geophysical Research (1896-1977)* 73, 6099-6110.

Lofi, J. (2018) *Seismic Atlas of the Messinian Salinity Crisis markers in the Mediterranean Sea - Volume 2.* Société Géologique de France.

Lugli, S., Manzi, V., Roveri, M. and Schreiber, B.C. (2010) The Primary Lower Gypsum in the Mediterranean: a new facies interpretation for the first stage of the Messinian salinity crisis. *Palaeogeography, Palaeoclimatology, Palaeoecology* 297, 83-99.

Lugli, S., Manzi, V., Roveri, M. and Schreiber, B.C. (2015) The deep record of the Messinian salinity crisis: Evidence of a non-desiccated Mediterranean Sea. *Palaeogeography, Palaeoclimatology, Palaeoecology* 433, 201-218.

Magnuson, E., Mykytczuk, N.C.S., Pellerin, A., Goordial, J., Twine, S.M., Wing, B., Foote, S.J., Fulton, K. and Whyte, L.G. (2020) Thiomicrorhabdus streamers and sulfur cycling in perennial hypersaline cold springs in the Canadian high Arctic. *Environ Microbiol.*

Manzi, V., Argnani, A., Corcagnani, A., Lugli, S. and Roveri, M. (2020) The Messinian salinity crisis in the Adriatic foredeep: Evolution of the largest evaporitic marginal basin in the Mediterranean. *Marine and Petroleum Geology* 115, 104288.

Markovic, S., Paytan, A., Li, H. and Wortmann, U.G. (2016) A revised seawater sulfate oxygen isotope record for the last 4Myr. *Geochimica et Cosmochimica Acta* 175, 239-251.

Masterson, A.L., Wing, B.A., Paytan, A., Farquhar, J. and Johnston, D.T. (2016) The minor sulfur isotope composition of Cretaceous and Cenozoic seawater sulfate. *Paleoceanography* 31, 779-788.

Melegy, A. and Ismael, I. (2013) Microstructure and geochemistry studies on Messinian gypsum deposits from the Northern Coast of Egypt. *Arabian Journal of Geosciences* 7.

Natalicchio, M., Birgel, D., Dela Pierre, F., Ziegenbalg, S., Hoffmann-Sell, L., Gier, S. and Peckmann, J. (2022) Messinian bottom-grown selenitic gypsum: An archive of microbial life. *Geobiology*.

Ochoa, D., Sierro, F.J., Lofi, J., Maillard, A., Flores, J.-A. and Suárez, M. (2015) Synchronous onset of the Messinian evaporite precipitation: First Mediterranean offshore evidence. *Earth and Planetary Science Letters* 427, 112-124.

Ono, S., Wing, B., Johnston, D., Farquhar, J. and Rumble, D. (2006) Mass-dependent fractionation of quadruple stable sulfur isotope system as a new tracer of sulfur biogeochemical cycles. *Geochimica et Cosmochimica Acta* 70, 2238-2252.

Orszag-Sperber, F., Caruso, A., Blanc-Valleron, M.-M., Merle, D. and Rouchy, J.M. (2009) The onset of the Messinian salinity crisis: Insights from Cyprus sections. *Sedimentary Geology* 217, 52-64.

Ortí, F., Rosell, L. and Anadón, P. (2010) Diagenetic gypsum related to sulfur deposits in evaporites (Libros Gypsum, Miocene, NE Spain). *Sedimentary Geology* 228, 304-318.

Panieri, G., Lugli, S., Manzi, V., Palinska, K.A. and Roveri, M. (2008) Microbial communities in Messinian evaporite deposits of the Vena del Gesso (northern Apennines, Italy). *Stratigraphy* 5, 343-352.

Pashko, P., Milushi, I. and Hoxha, V. (2019) THE MESSINIAN EVAPORITES OF THE PREADRIATIC FORELAND BASIN (ALBANIA).

Pellerin, A., Bui, T.H., Rough, M., Mucci, A., Canfield, D.E. and Wing, B.A. (2015) Mass-dependent sulfur isotope fractionation during reoxidative sulfur cycling: A case study from Mangrove Lake, Bermuda. *Geochimica et Cosmochimica Acta* 149, 152-164.

Pierre, C. (1982) Teneurs en isotopes stables (^{18}O , ^2H , ^{34}S , ^{36}S) et conditions de g n se des  vaporites marines: application   quelques milieux actuels et au Messinien de la M diterran e.  diteur inconnu.

Raab, M., Friedman, G.M., Spiro, B., Starinsky, A. and Zak, I. (1997) The geological history of Messinian (upper miocene) evaporites in the Central Jordan Valley (Israel) and how strontium and sulfur isotopes relate to their origin. *Carbonates and Evaporites* 12, 296-324.

Raab, M. and Spiro, B. (1991) Sulfur isotopic variations during seawater evaporation with fractional crystallization. *Chemical Geology: Isotope Geoscience section* 86, 323-333.

Raad, F., Lofi, J., Maillard, A., Tzevahirtzian, A. and Caruso, A. (2021) The Messinian Salinity Crisis deposits in the Balearic Promontory: An undeformed analog of the MSC Sicilian basins?? *Marine and Petroleum Geology* 124, 104777.

Robertson, A.H.F., Eaton, S., Follows, E.J. and Payne, A.S. (1995) Depositional processes and basin analysis of Messinian evaporites in Cyprus. *Terra Nova* 7, 233-253.

Rouchy, J.M., Caruso, A., Pierre, C., Blanc-Valleron, M.-M. and Bassetti, M.A. (2007) The end of the Messinian salinity crisis: Evidences from the Chelif Basin (Algeria). *Palaeogeography, Palaeoclimatology, Palaeoecology* 254, 386-417.

Rouchy, J.M. and Monty, C.L. (1981) Stromatolites and Cryptalgal Laminites Associated with Messinian Gypsum of Cyprus, in: Monty, C. (Ed.), *Phanerozoic Stromatolites*. Springer Berlin Heidelberg, Berlin, Heidelberg, pp. 155-180.

Sakai, H. (1971) Sulfur and oxygen isotopic study of barite concretions from banks in the Japan Sea off the Northeast Honshu, Japan. *GEOCHEMICAL JOURNAL* 5, 79-93.

Schopf, J.W., Farmer, J.D., Foster, I.S., Kudryavtsev, A.B., Gallardo, V.A. and Espinoza, C. (2012) Gypsum-permineralized microfossils and their relevance to the search for life on Mars. *Astrobiology* 12, 619-633.

Seitaj, D., Schauer, R., Sulu-Gambari, F., Hidalgo-Martinez, S., Malkin, S.Y., Burdorf, L.D.W., Slomp, C.P. and Meysman, F.J.R. (2015) Cable bacteria generate a firewall against euxinia in seasonally hypoxic basins. *Proceedings of the National Academy of Sciences* 112, 13278-13283.

Sghari, A. (2012) Un dépôt évaporitique du Miocène supérieur dans le Sud tunisien : une conséquence de la crise messinienne ? *Géomorphologie : relief, processus, environnement* 18, 279-294.

Sim, M.S., Bosak, T. and Ono, S. (2011a) Large sulfur isotope fractionation does not require disproportionation. *Science* 333, 74-77.

Sim, M.S., Ono, S., Donovan, K., Templer, S.P. and Bosak, T. (2011b) Effect of electron donors on the fractionation of sulfur isotopes by a marine *Desulfovibrio* sp. *Geochimica et Cosmochimica Acta* 75, 4244-4259.

Tekin, E., Varol, B. and Ayyıldız, T. (2010) Sedimentology and paleoenvironmental evolution of Messinian evaporites in the Iskenderun–Hatay basin complex, Southern Turkey. *Sedimentary Geology* 229, 282-298.

Thamdrup, B., Finster, K., Hansen, J.W. and Bak, F. (1993) Bacterial Disproportionation of Elemental Sulfur Coupled to Chemical Reduction of Iron or Manganese. *Applied and Environmental Microbiology* 59, 101-108.

Thode, H.G. and Monster, J. (1965) Sulfur-Isotope Geochemistry of Petroleum, Evaporites, and Ancient Seas¹, in: Young, A., Galley, J.E. (Eds.), *Fluids in Subsurface Environments*. American Association of Petroleum Geologists, p. 0.

Topper, R., Lugli, S., Manzi, V., Roveri, M. and Meijer, P. (2014) Precessional control of Sr ratios in marginal basins during the Messinian Salinity Crisis. *Geochemistry, Geophysics, Geosystems*.

Topper, R.P.M., Flecker, R., Meijer, P.T. and Wortel, M.J.R. (2011) A box model of the Late Miocene Mediterranean Sea: Implications from combined ⁸⁷Sr/⁸⁶Sr and salinity data. *Paleoceanography* 26.

Topper, R.P.M. and Meijer, P.T. (2015) The precessional phase lag of Messinian gypsum deposition in Mediterranean marginal basins. *Palaeogeography, Palaeoclimatology, Palaeoecology* 417, 6-16.

Tostevin, R., Turchyn, A.V., Farquhar, J., Johnston, D.T., Eldridge, D.L., Bishop, J.K.B. and McIlvin, M. (2014) Multiple sulfur isotope constraints on the modern sulfur cycle. *Earth and Planetary Science Letters* 396, 14-21.

Tudge, A.P. and Thode, H.G. (1950) THERMODYNAMIC PROPERTIES OF ISOTOPIC COMPOUNDS OF SULPHUR. *Canadian Journal of Research* 28b, 567-578.

- Turchyn, A.V. and Schrag, D.P. (2004) Oxygen Isotope Constraints on the Sulfur Cycle over the Past 10 Million Years. *Science* 303, 2004.
- Utrilla, R., Pierre, C., Orti, F. and Pueyo, J.J. (1992) Oxygen and sulphur isotope compositions as indicators of the origin of Mesozoic and Cenozoic evaporites from Spain. *Chemical Geology* 102, 229-244.
- Van Driessche, A., Canals, A., Ossorio, M., Reyes, R.C. and García-Ruiz, J.M. (2016) Unraveling the Sulfate Sources of (Giant) Gypsum Crystals Using Gypsum Isotope Fractionation Factors. *The Journal of Geology* 124, 235-245.
- Zerkle, A.L., Farquhar, J., Johnston, D.T., Cox, R.P. and Canfield, D.E. (2009) Fractionation of multiple sulfur isotopes during phototrophic oxidation of sulfide and elemental sulfur by a green sulfur bacterium. *Geochimica et Cosmochimica Acta* 73, 291-306.
- Zerkle, A.L., Jones, D.S., Farquhar, J. and Macalady, J.L. (2016) Sulfur isotope values in the sulfidic Frasassi cave system, central Italy: A case study of a chemolithotrophic S-based ecosystem. *Geochimica et Cosmochimica Acta* 173, 373-386.
- Zhang, J.-Z. and Millero, F.J. (1993) The products from the oxidation of H₂S in seawater. *Geochimica et Cosmochimica Acta* 57, 1705-1718.

